THE MACHO PROJECT: MICROLENSING RESULTS FROM 5.7 YEARS OF LARGE MAGELLANIC CLOUD OBSERVATIONS

C. ALCOCK,[1,2] R. A. ALLSMAN,[3] D. R. ALVES,[4] T. S. AXELROD,[5] A. C. BECKER,[6] D. P. BENNETT,[7,1] K. H. COOK,[1,2]
N. DALAL,[2,8] A. J. DRAKE,[1,5] K. C. FREEMAN,[5] M. GEHA,[1] K. GRIEST,[2,8] M. J. LEHNER,[9] S. L. MARSHALL,[1,2]
D. MINNITI,[1,10] C. A. NELSON,[1,11] B. A. PETERSON,[5] P. POPOWSKI,[1] M. R. PRATT,[6] P. J. QUINN,[12]
C. W. STUBBS,[2,5,6,13] W. SUTHERLAND,[14] A. B. TOMANEY,[6] T. VANDEHEI,[2,8] AND D. WELCH[15]
(THE MACHO COLLABORATION)

ABSTRACT

We report on our search for microlensing toward the Large Magellanic Cloud (LMC). Analysis of 5.7 yr of photometry on 11.9 million stars in the LMC reveals 13–17 microlensing events. A detailed treatment of our detection efficiency shows that this is significantly more than the ~ 2–4 events expected from lensing by known stellar populations. The timescales ($\hat{t}$) of the events range from 34 to 230 days. We estimate the microlensing optical depth toward the LMC from events with $2 < \hat{t} < 400$ days to be $\tau_2^{400} = 1.2^{+0.4}_{-0.3} \times 10^{-7}$, with an additional 20% to 30% of systematic error. The spatial distribution of events is mildly inconsistent with LMC/LMC disk self-lensing, but is consistent with an extended lens distribution such as a Milky Way or LMC halo. Interpreted in the context of a Galactic dark matter halo, consisting partially of compact objects, a maximum-likelihood analysis gives a MACHO halo fraction of 20% for a typical halo model with a 95% confidence interval of 8%–50%. A 100% MACHO halo is ruled out at the 95% confidence level for all except our most extreme halo model. Interpreted as a Galactic halo population, the most likely MACHO mass is between 0.15 and 0.9 $M_\odot$, depending on the halo model, and the total mass in MACHOs out to 50 kpc is found to be $9^{+4}_{-3} \times 10^{10}$ $M_\odot$, independent of the halo model. These results are marginally consistent with our previous results, but are lower by about a factor of 2. This is mostly due to Poisson noise, because with 3.4 times more exposure and increased sensitivity to long-timescale events, we did not find the expected factor of ~ 4 more events. In addition to a larger data set, this work also includes an improved efficiency determination, improved likelihood analysis, and more thorough testing of systematic errors, especially with respect to the treatment of potential backgrounds to microlensing. We note that an important source of background are supernovae (SNe) in galaxies behind the LMC.

Subject headings: dark matter — Galaxy: halo — Galaxy: structure — gravitational lensing — stars: low-mass, brown dwarfs — white dwarfs

On-line material: Color figures

1. INTRODUCTION

Following the suggestion of Paczyński (1986), several groups are now engaged in searches for dark matter in the form of massive compact halo objects (MACHOs) using gravitational microlensing, and many candidate microlensing events have been reported. Reviews of microlensing in this context are given by Paczyński (1996) and Roulet & Mollerach (1996).

Previously (Alcock et al. 1997a), we conducted an analysis of 2.1 yr of photometry of 8.5 million stars, and found 6–8 microlensing events, implying an optical depth toward the LMC of $2.9^{+1.4}_{-0.9} \times 10^{-7}$ for the 8 event sample and $2.1^{+1.1}_{-0.7} \times 10^{-7}$ for the 6 event sample (Alcock et al. 1996a, 1997a; hereafter A96 and A97, respectively). Interpreted as evidence for a MACHO contribution to the Milky Way dark halo, this implied a MACHO mass out to 50 kpc

[1] Lawrence Livermore National Laboratory, Livermore, CA 94550; alcock@igpp.llnl.gov, kcook@igpp.llnl.gov, adrake@igpp.llnl.gov, mgeha@igpp.llnl.gov, stuart@igpp.llnl.gov, dminniti@igpp.llnl.gov, cnelson@igpp.llnl.gov, popowski@igpp.llnl.gov.
[2] Center for Particle Astrophysics, University of California, Berkeley, CA 94720.
[3] Supercomputing Facility, Australian National University, Canberra, ACT 0200, Australia; Robyn.Allsman@anu.edu.au.
[4] Space Telescope Science Institute, 3700 San Martin Drive, Baltimore, MD 21218; alves@stsci.edu.
[5] Research School of Astronomy and Astrophysics, Canberra, Weston Creek, ACT 2611, Australia; tsa@mso.anu.edu.au, kcf@mso.anu.edu.au, peterson@mso.anu.edu.au.
[6] Departments of Astronomy and Physics, University of Washington, Seattle, WA 98195; becker@astro.washington.edu, stubbs@astro.washington.edu.
[7] Department of Physics, University of Notre Dame, Notre Dame, IN 46556; bennett@bustard.phys.nd.edu.
[8] Department of Physics, University of California at San Diego, San Diego, CA 92093; endall@physics.ucsd.edu, kgriest@ucsd.edu, vandehei@astrophys.ucsd.edu.
[9] Department of Physics, University of Sheffield, Sheffield S3 7RH, England, UK; m.lehner@sheffield.ac.uk.
[10] Departimento de Astronomia, P. Universidad Catolica, Casilla 104, Santiago 22, Chile; dante@astro.puc.cl.
[11] Department of Physics, University of California at Berkeley, Berkeley, CA 94720.
[12] European Southern Observatory, Karl Schwarzschild Strasse 2, D-8574 8 Gärching bei München, Germany; pjq@eso.org.
[13] Visiting Astronomer, Cerro Tololo Inter-American Observatory.
[14] Department of Physics, University of Oxford, Oxford OX1 3RH, England, UK; w.sutherland@physics.ox.ac.uk.
[15] McMaer University, Hamilton, Ontario Canada L8S 4M1; welch@physics.mcmaer.ca.

of $2.0^{+1.2}_{-0.7} \times 10^{11} M_\odot$. Depending on the halo model, this meant a MACHO halo fraction of between 15% and 100%, and a typical MACHO mass of 0.1–1 $M_\odot$ (A97; Gates, Gyuk, & Turner 1995). The EROS group has reported two candidates (Aubourg et al. 1993; Renault et al. 1997), which they interpreted as limiting the number of MACHOs with masses less than 0.8 $M_\odot$ to less than 100%. Recently, the EROS updated and expanded survey, EROS II, has made a preliminary report on two new events that they interpret as limiting the number of MACHOs with masses less than 1 $M_\odot$ in a standard halo to less than 60% (Lasserre et al. 1999). These limits cut through the A97 likelihood contours, but are consistent with the results of this paper. The OGLE (Udalski, Kubiak, & Szymański 1997) collaboration also reported one LMC microlensing event in 1999. All claimed LMC events have characteristic timescales between $\hat{t} \sim 34$ and 230 days, while searches for short-timescale events with timescales 1 hr $\lesssim \hat{t} \lesssim 10$ days have revealed no candidates to date (Aubourg et al. 1995; Alcock et al. 1996b, 1998), allowing important limits to be set on low-mass dark matter. In addition, two candidates have been observed toward the SMC (Alcock et al. 1997b, 1999a; Albrow et al. 1999; Palanque-Delabrouille et al. 1998; Afonso et al. 1999, 2000; Rhie et al. 1999; Udalski et al. 1998), but the small number of events, the location of the lenses, and the large expected SMC self-lensing rate reduce their usefulness as a probe of the dark halo.

Conclusions based on our previous work suffered from Poisson error as a result of the small number of events. Increasing the time span monitored from 2.1 to 5.7 yr and increasing the number of monitored fields from 22 to 30 gives 13–17 events (depending on the selection criteria used), as well as greatly increasing our sensitivity to long-duration events and therefore to higher mass MACHOs. It also increases coverage over the face of the LMC, providing a useful tool for distinguishing between various interpretations of the microlensing events. In addition, while our previous analyses contained the most careful evaluations of microlensing detection efficiency ever done, we have made several important improvements, and have thoroughly tested the robustness of our methods. In addition, we have more fully and carefully investigated sources of potential background to microlensing, in particular the LMC variable star background (i.e., bumpers; A97) and supernovae (SNe) in galaxies behind the LMC. For example, one candidate event classified in A97 as microlensing (LMC 10) is now removed as a probable background SN.

The nature of microlensing implies that many of our events will have low signal-to-noise ratio (S/N), so to test the robustness of our results and to estimate systematic error due to our event-selection methodology, we present two independently derived sets of selection criteria ("cuts"), with two corresponding sets of events and efficiency determinations. One set is designed to select only high-S/N events and is modeled on the selection criteria used in A97. The other is designed to be inclusive of lower S/N events and also exotic microlensing events, and makes heavier use of several new statistics. While the number of microlensing candidate events selected by the two sets of cuts differ, the corresponding efficiencies compensate, and the resulting optical depth values, halo fractions, etc., are essentially the same. This suggests that the systematic error in our optical depth, etc., due to our choice of cuts is small. Finally, we implement an improved likelihood analysis that self-

consistently incorporates currently available information on known stellar backgrounds.

The increase in the number of events, improved efficiency determination, and more thorough investigation of systematic errors and backgrounds, such as bumpers and SNe, makes the results of this paper the most accurate to date. At this point, uncertainties in the model of the Milky Way and the model of the LMC dominate both the quantitative and the interpretational aspects of microlensing as a probe of dark matter.

The plan of the paper is as follows. In § 2 we outline the observations and photometric reductions. In § 3 we describe our microlensing event selection criteria, present the resulting candidates, and discuss several sources of background to microlensing, including bumpers and SNe. In § 4 we estimate our detection efficiency, which has been improved in a number of ways. In § 5 we show the distributions of the selected events in the color-magnitude diagram (CMD), location on the sky, and impact parameter. We compare with predicted distributions, thereby testing the microlensing hypothesis. In § 6 we provide various analyses of the sample. We calculate the optical depth, and discuss why it is a factor of 2 smaller than in A97. We perform a likelihood analysis that explicitly includes models of the Milky Way and LMC stellar populations to find new estimates of the MACHO contribution to the dark halo and the number of expected events from known stellar populations. We find new favorable mass ranges for the lenses if they are halo objects. We also discuss various interpretations of our results, including the possibility that no MACHOs exist and all the lensing is due to stellar lenses.

Note that many of the reduction and analysis procedures used here are very similar to those in A96 and A97, to which we refer extensively. A more rigorous description of our detection efficiency, which is only briefly outlined in this paper, may be found in the companion paper, Alcock et al. (2000b), and in Vandehei (2000). The reader is encouraged to consult these papers to understand the details of the experiment, but we repeat the main points here for clarity.

2. OBSERVATIONS AND PHOTOMETRIC REDUCTIONS

The MACHO Project has had full-time use of the 1.27 m telescope at Mount Stromlo Observatory, Australia, since 1992 July. Observations were completed at the end of 1999 December. Details of the telescope system are given by Hart et al. (1996), and details of the camera system by Stubbs et al. (1993) and Marshall et al. (1994). Briefly, corrective optics and a dichroic are used to give simultaneous imaging of a $42' \times 42'$ field in two colors, using eight 2048^2 pixel CCDs. As of 1998 March, over 70,000 exposures had been taken with the system, over 5 Tbytes of raw image data. About 55% are of the LMC; the rest are of fields in the Galactic center and SMC.

In this paper, we consider the first 5.7 yr of data from 30 well-sampled fields, located in the central $5° \times 3°$ of the LMC; field centers are listed in Table 1 and shown in Figure 1.

The observations described here comprise 21,570 images distributed over the 30 fields. These include most of our observations of these fields in the time span of 2067 days from 1992 September 18 to 1998 March 17, as well as a fraction of our observations taken between 1992 July 22 and 1992 August 23, when our system was still in an engineering phase. The mean number of exposures per field is

TABLE 1

FIELD CENTERS

| FIELD | CENTER | | OBSERVATIONS |
	R.A. (2000)	Decl. (2000)	
1	05 05 23	−69 05 24	1017
2	05 12 47	−68 30 21	860
3	05 22 24	−68 28 01	720
5	05 11 17	−69 40 18	839
6	05 20 00	−70 17 10	856
7	05 28 54	−70 27 31	1027
9	05 10 57	−70 23 40	811
10	05 04 34	−69 52 19	665
11	05 36 56	−70 31 34	930
12	05 45 36	−70 35 16	772
13	05 19 39	−70 51 40	752
14	05 35 53	−71 09 22	741
15	05 45 34	−71 14 36	718
17	04 57 04	−69 43 11	345
18	04 57 55	−68 56 08	594
19	05 06 09	−68 21 03	672
22	05 11 18	−71 00 19	398
23	05 02 51	−70 35 39	339
24	05 00 39	−67 56 45	297
47	04 53 05	−68 01 26	610
53	05 02 09	−66 40 19	180
55	05 02 15	−65 58 50	241
57	05 09 07	−65 46 07	189
76	05 44 13	−69 49 41	386
77	05 27 24	−69 45 24	1338
78	05 19 26	−69 42 27	1312
79	05 12 59	−69 05 43	1226
80	05 22 44	−69 05 18	1186
81	05 35 56	−69 49 34	792
82	05 32 50	−69 03 18	757

NOTE.—This table lists the 30 well-sampled fields used in the current analysis. The eight new fields are 17, 22, 23, 24, 53, 55, 57, and 76; these typically have less than half the observations of the top 22 fields. We observe 82 LMC fields in total, but the remaining 52 were observed less often (∼120 observations each).

21570/30 = 719, with a range from 180 to 1338. The sampling varies between fields (Table 1), since the higher priority fields were often observed twice per night, with an average of about 4 hr between exposures.

The photometric reduction procedure was very similar to that described in A96 and A97; briefly, a good-quality image of each field is chosen as a template and used to generate a list of stellar positions and magnitudes. The templates are used to "warm-start" all subsequent photometric reductions, and for each star we record information on the flux, an error estimate, the object type, the χ^2 of the point-spread function (PSF) fit, a crowding parameter, a local sky level, and the fraction of the star's flux rejected due to bad pixels and cosmic rays. Details of the MACHO image data and photometry code (SoDoPHOT) are provided in Alcock et al. (1999b). The resulting data are reorganized into light curves and searched for variable stars and microlensing events. The LMC 5.7 yr photometry database is about 200 Gbytes in size.

For the 22 fields reported on in A97, we have well calibrated photometry (Alcock et al. 1999b), but for the eight new fields our photometry has been only roughly calibrated on a global basis (see § 2 in A97). Event selection is generally based on this rough calibration, but as noted below, we

report the well-calibrated magnitudes and colors when possible.

We have corrected a minor complication in A97, where for software-related reasons we used different templates for the first and second year's reductions of six of our fields.[16] For these fields there was not a one-to-one correspondence between the set of stars in the two distinct years used, and the first and second years had to be analyzed separately. All photometry in these six fields have been rerun using the new generation of templates, and the light curves have now been merged onto a common photometric system.

3. EVENT DETECTION

The data set used here consists of about 256 billion individual photometric measurements. Discriminating genuine microlensing from stellar variability, background, and systematic photometry errors is difficult, and the significance of the results depends on the event-selection criteria.

The selection criteria should accept "true" microlensing events and reject events due to intrinsic stellar variability and instrumental effects. The determination of our event-selection criteria could not be made before looking in detail at the light curves. We had to discover various background sources and learn how to perform event selection from the data we gather themselves, making the selection criteria dependent on the data. As much as possible, we have tried to base the selection criteria on our Monte Carlo artificial events (see § 4). Although this allows us to place cuts along natural breaks in parameter space (which lessens the sensitivity of the final results on the exact placement of the cut), it did not allow us to fully explore the background of variable stars. This adds some subjectivity to our analysis, which we quantify below by considering two limiting cases.

For each light curve, we compute a set of over 150 temporal variability statistics. We use two levels of statistics: level 1 statistics are calculated for all stars, while level 2 statistics are calculated only for those stars that pass the level 1 selection criteria. We have developed selection criteria ("cuts") that use the level 2 statistics to distinguish microlensing from backgrounds such as variable stars and noise. The selection criteria have evolved over the course of the experiment. As the volume of data on a light curve increases, the meaning of some statistics change in subtle ways. Thus, one must be careful not to blindly apply selection criteria from one data set to another. For example, a fitted χ^2 to a constant-flux star over 2.1 yr of data will not necessarily be the same when computed using 5.7 yr of data, due to changes in weather patterns (and thus seeing and sky level) and the CCD camera over the course of the experiment. In addition, in order to increase our sensitivity to low-S/N and exotic microlensing, our level 1 criteria (see below) have been loosened relative to those used in A97. This means that our set of level 1 candidates contains more variable stars and other noisy events, thus requiring changes to the final level 2 selection criteria. Because of the changes in the level 1 criteria, the selection criteria used in A97 are no longer appropriate for the 5.7 yr data. About 45 light curves, 26 of which are clearly noise or variable stars, would pass the A97 criteria applied to the current data.

We select the events using two different and independently developed sets of level 2 selection criteria. This allows us
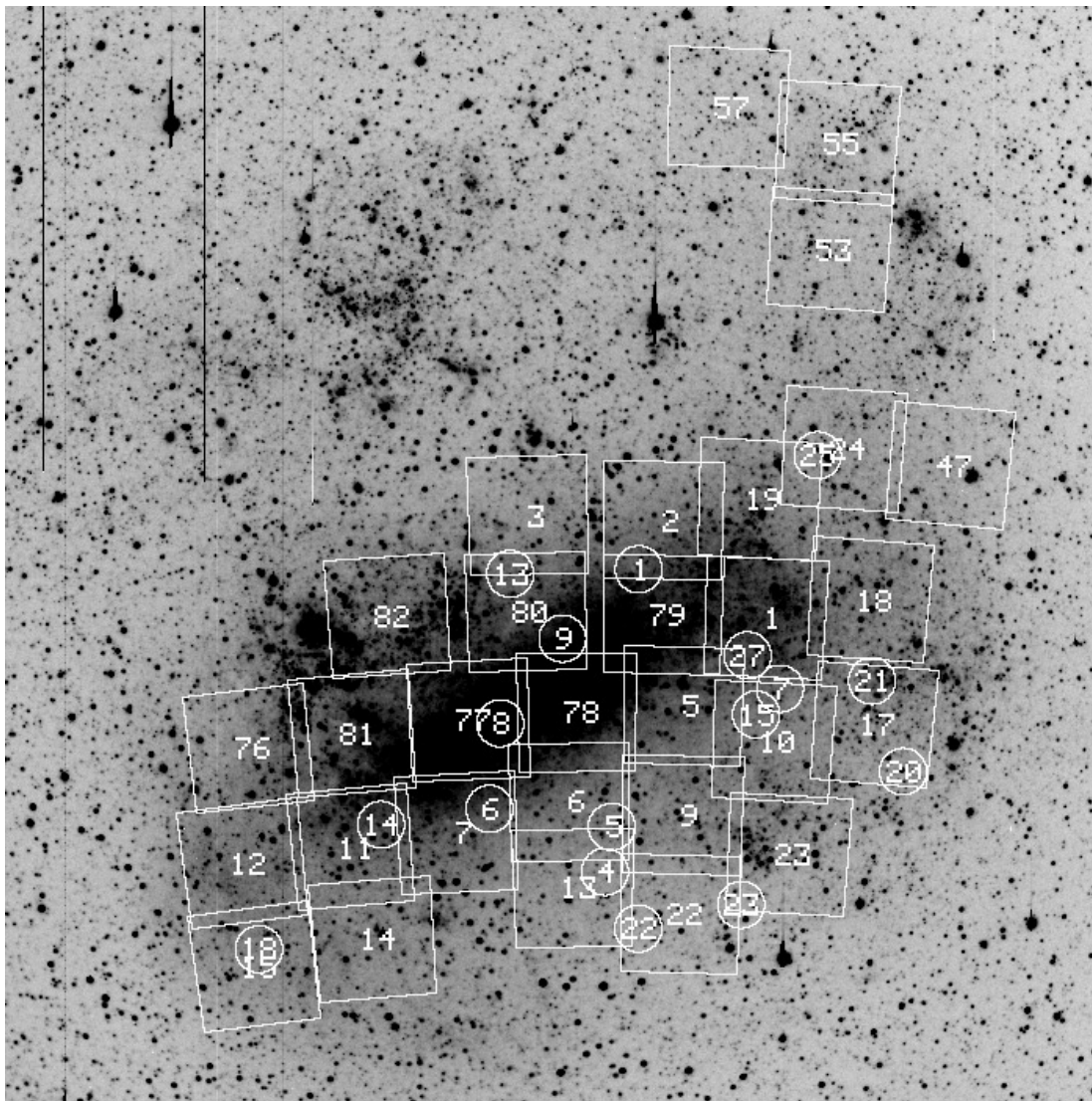
---

[16] Fields 1, 7, 9, 77, 78, and 79.

Fig. 1.—*R*-band image of the LMC, 8°2 on a side (G. Bothun 1997, private communication), showing the locations of the 30 MACHO fields used here. Also shown are the locations of the 17 microlensing candidates discussed in the text. See the electronic edition of the Journal for a color version of this figure.

to explore possible systematic error due to the choice of cuts. While the goal of both sets of cuts is to select as many microlensing light curves as possible, while rejecting as many nonmicrolensing light curves as possible, the two sets of cuts were explicitly developed with complementary philosophies in mind. The first set of selection criteria (hereafter referred to as "criteria set A" or more simply, "set A") was designed to be rather tight, only accepting events with a single highly significant bump in either passband, while requiring the baseline to remain very flat, as expected in simple microlensing. These cuts resemble those in A97, and for the most part statistics similar to those described in A97 were employed. The second set of selection criteria (criteria set B) was designed to be rather loose, in an attempt to search for exotic or low-S/N microlensing candidates. This second set of cuts also looked for a single significant bump in either passband with a flat baseline, but made use of some new statistics not available in A97. The new statistics (described below) better characterize and filter out some variable stars and noisy events. To conservatively estimate the subjective nature of our event selection, marginal events

suspected of being SNe, etc., are preferentially rejected from set A, but kept in set B.

Note that as long as the experiment's event-detection efficiency is calculated properly, and the selection criteria are sufficiently stringent to accept only real microlensing events, changes in the selection criteria should be accounted for in the efficiency calculations, and the details should not greatly affect the final results (in the limit of a large number of detected events). This statement implicitly ignores exotic microlensing events such as binary lens or parallax microlensing events that have light curves that differ from those used in our efficiency determination. We have not determined our efficiency for exotic events, but selection criteria set B is designed, in part, to be more sensitive to such events. Furthermore, a much more sensitive search for exotic lensing events has been carried out, and none were found. Therefore, we do expect that the difference between selection criteria sets A and B is a reasonable indication of our selection criteria systematic error, and we find that this difference is fairly small, as outlined here and discussed in § 6.

We have summarized the old (A97) and new selection

criteria sets (A and B) in Tables 2 and 3. In § 3.1 we briefly describe some of the analysis and statistics used in applying these selection criteria, and in § 3.2 we present the set of events selected by criteria sets A and B. In § 3.3 we identify two main sources of background to microlensing and discuss how they can be removed from the true microlensing pool. Finally, in § 3.4 we remove our identified background events and summarize the final sets of microlensing candidates (the final sets A and B) used to compute the results of this paper.

3.1. Selection Criteria Statistics

Photometric measurements with questionable PSF fit, too much crowding, missing pixels, or cosmic rays are flagged as suspect and removed from further consideration. The event detection then proceeds in two stages. The first stage, defining a level 1 collection of candidate events, is similar to that described in A97; a set of matched filters of timescales 7, 15, 45, and 100 days is run over each light curve. If, after convolution, a light curve shows a peak above a predefined significance level in either color, it is defined as a level 1 candidate. We also make use of a new filter that looks for bumps of any duration and add these light curves to the level 1 pool of candidates. (We found no additional candidates by this addition, however.) For level 1 candidates, a full 5 parameter fit to microlensing is made, and many level 2 statistics describing the significance of the peak, goodness of fit, etc., are calculated. We use the standard point-source–point-lens approximation (Refsdal 1964; A96). The five free parameters of the fit are the baseline flux in red and blue passbands, f_{0R} and f_{0B}, respectively, and the three parameters of the microlensing event: the minimum impact parameter in units of the Einstein radius, u_{min}, the Einstein diameter crossing time, $\hat{t} \equiv 2r_E/v_\perp$, and the time of maximum magnification, t_{max}. Later, instead of u_{min} we will often use the fit maximum magnification, $A_{max} \equiv A(u_{min})$, which is more closely related to the observed light curve.

Light curves passing loose cuts on these statistics are defined as "level 1.5" candidates, and are output as individual files along with their associated statistics. In the present analysis, there are approximately 150,000 level 1.5 candidates, the vast majority of which are variable stars or noisy light curves.

Table 2 gives a list of statistics used in selecting microlensing, and Table 3 lists the specifics of the old (A97) and the two new (A and B) sets of cuts. A more detailed description of some of the new statistics and the rationale for them are given in the Appendix. We now summarize some of the changes made since A97.

Our set A selection criteria are designed to accept high-quality microlensing candidates, while using mainly the statistics described in A97. Some of the cuts on these statistics have been loosened as we have developed a better understanding of our variable-star background; for example, the cut on magnification was loosened from $A_{max} > 1.75$ to its present value of $A_{max} > 1.49$, because our main background of variable stars, a class of blue variables called bumpers (see below), almost never show fit magnifications larger than 1.5 and are well isolated in the CMD. We also loosened our main significance cut, $\Delta\chi^2/(\chi^2_{ml}/N_{dof}) < 400$ (from 500 in A97) because a number of other statistics were tightened. These include $A_{max} > 3\bar{\sigma}$ (from $2\bar{\sigma}$, where $\bar{\sigma}$ is the average red/blue error in magnitudes), which is a S/N cut; $\chi^2_{ml\text{-}out}/N_{dof} < 1.8$ to reject variables (from < 4.0 in A97); and $\Delta\chi^2/(\chi^2_{peak}/N_{dof}) > 350$ (from > 200 in A97), another S/N cut. This later cut is somewhat more reliant on the shape of the 5 parameter microlensing fit and increases the likelihood of rejecting exotic microlensing; for this reason, criteria set B below does not use this cut.

Our set B selection criteria are designed to accept any light curves with a significant unique peak and a fairly flat baseline. Selection criteria set B is summarized in Figure 2, which illustrates our two most important S/N cuts: the cut on magnification, A_{max}, and the cut on $\Delta\chi^2/(\chi^2_{peak}/N_{dof})$. Events that passed the basic cuts (all cuts used by criteria set B minus the ordinate and abscissa cuts of Fig. 2) are shown as filled circles and labeled. The final cuts on magnification, A_{max}, and $\Delta\chi^2/(\chi^2_{peak}/N_{dof})$ are shown as solid lines (for comparison, dotted lines showing criteria set A are also plotted). Open circles indicate events that fail criteria set B's bumper cut, and filled squares show events that fail criteria set B's uniqueness cut. The new statistics on the

TABLE 2
BRIEF DESCRIPTION OF STATISTICS

Statistic	Description
bmr$N$	Number of simultaneous red/blue observations
rN	Number of red observations
bN	Number of blue observations
crdrej	Fraction of observations rejected due to high crowding
pkcrdrej	Fraction in peak ($t_{max} \pm 1.0\hat{t}$) rejected due to high crowding
pkpsfrej	Fraction in peak ($t_{max} \pm 1.0\hat{t}$) rejected due to bad PSF
bauto/rauto	Ratio of blue power to red power
pfwsr	Ratio of blue power to red power (simultaneous points only)
rbcrossout	Red/blue cross-correlation statistic
N_{hi}/N_{pk}	Fraction of points in peak ($t_{max} \pm 1.0\hat{t}$) above median flux
χ^2_{ml-out}/N_{dof}	Reduced χ^2 of constant flux fit outside the peak ($t_{max} \pm 2.0\hat{t}$)
$\chi^2_{robust-out}/N_{dof}$	Robust reduced χ^2 of constant flux fit outside the peak ($t_{max} \pm 1.0\hat{t}$)
$\Delta\chi^2/(\chi^2_{peak}/N_{dof})$	Improvement in χ^2 of simple microlensing over constant flux in peak region ($A_{max} > 1.1$)
$\Delta\chi^2/(\chi^2_{ml}/N_{dof})$	Improvement in χ^2 of simple microlensing over constant flux (all data)
pfrdev2	Second peak significance statistics
$\Delta\chi^2_{SN-ml}$	Improvement in χ^2 of blended microlensing fit over SN Ia fit
f_{CRD}	Average red and blue crowding measure
$\bar{\sigma}$	Average red and blue photometric error in magnitudes

<div align="center">

TABLE 3

SELECTION CRITERIA

</div>

| Description	Year 2 (A97)	Criteria A	Criteria B
Minimum coverage......	$\mathrm{bmr}N \geq 7 > 40$ baseline points, $\hat{t} < 300$	$rN > 0$ and $bN > 0 > 45$ baseline points, $\hat{t} < 600$, $t_{max} > 310$	> 65 simultaneous baseline points, $\hat{t} < 600$, $t_{max} > 310$
SN 87A echo.............	$10' \times 10'$ square excluded	$10' \times 10'$ square excluded	$10' \times 10'$ square excluded
Crowd and PSF.........	$f_{\mathrm{CRD}} < [\Delta\chi^2/(\chi^2/N_{dof})]^{10/9}/520$ and crdrej < 0.05	None	pkcrdrej + pkpsfrej < 0.2
Bumper cut..............	$V > 17.5$ and $V - R < 0.9$	$V > 17.5$ and $V - R < 0.9$	$V > 17$ and ($A_{max} > 1.75$ or $V > 19$ or $V - R > 0.4$)
Variable cut..............	None	bauto/rauto > 0.75	pfwsr > 0.6 and rbcrossout < 0.75
High points..............	6 points $> 2\sigma$ and ≥ 1 point on rise and fall	7 points $> 2\sigma$	10 points $> 2\sigma$ and $N_{hi}/N_{pk} > 0.9$
Baseline fit...............	$\chi^2_{ml-out}/N_{dof} < 4$	$\chi^2_{ml-out}/N_{dof} < 1.8$	$\chi^2_{ml-out}/N_{dof} < 4$ and $\chi^2_{robust-out}/N_{dof} < 1.5$
Second S/N..............	$\Delta\chi^2/(\chi^2_{peak}/N_{dof}) > 200$	$\Delta\chi^2/(\chi^2_{peak}/N_{dof}) > 350$	None
Main S/N.................	$\Delta\chi^2/(\chi^2_{ml}/N_{dof}) > 500$	$\Delta\chi^2/(\chi^2_{ml}/N_{dof}) > 400$	$\Delta\chi^2/(\chi^2_{ml}/N_{dof}) > 300$
Magnification............	$A_{max} > \max(1.75, 1 + 2\bar{\sigma})$	$A_{max} > \max(1.49, 1 + 3\bar{\sigma})$	$A_{max} > \max(1.34, 1 + 4\bar{\sigma})$
Second peak.............	None	None	pfrdev2 < 90
Supernova cut...........	By eye	$\Delta\chi^2_{SN-ml} > 0$ and not event 22	$\Delta\chi^2_{SN-ml} > 0$
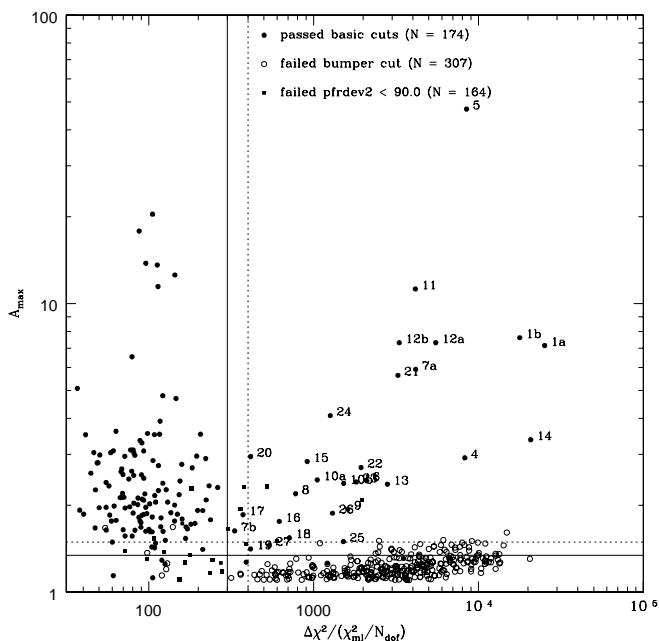
FIG. 2.—Illustration of the cuts used to select microlensing candidates for criteria set B. The x-axis is $\Delta\chi^2/(\chi^2_{ml}/N_{dof})$, where $\Delta\chi^2 \equiv \chi^2_{const} - \chi^2_{ml}$ is the improvement in χ^2 between a constant-brightness fit and a microlensing fit. The y-axis is the fitted maximum magnification. The 29 light curves are shown as filled circles and are labeled. The remaining symbols are explained in the figure and in detail in § 3.2. The solid lines show the final cuts for criteria set B. The dotted lines show the same for criteria set A. See text for details. See the electronic edition of the Journal for a color version of this figure.
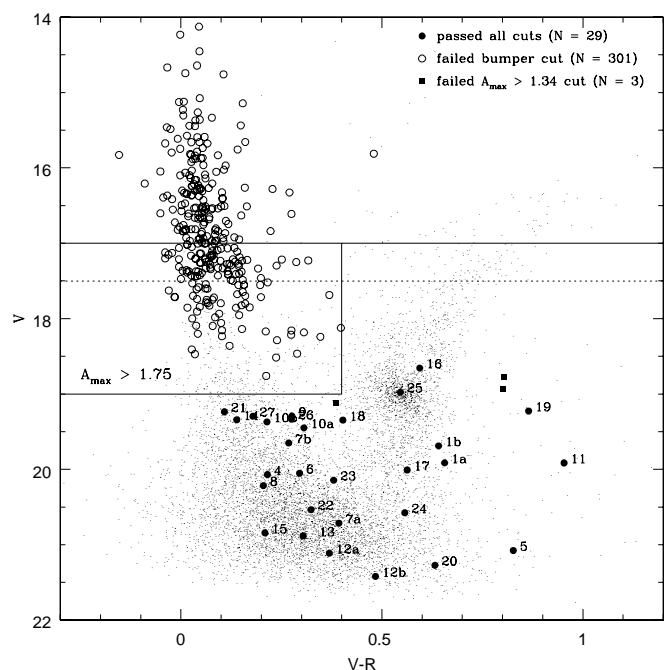

FIG. 3.—Illustration of the cuts used to select microlensing candidates for criteria set B in the CMD. The 29 light curves are shown as filled circles and are labeled. The "bumper" cut is outlined with solid lines and labeled with "$A_{max} > 1.75$" for criteria set B. The dotted lines show the same for criteria set A. The symbols are explained in the figure and in detail in § 3.3.1. The magnitudes displayed here use the rough global calibrations described in § 2. See the electronic edition of the Journal for a color version of this figure.

number of points rejected in the peak region, pkpsfrej + pkcrdrej, and the fraction of points above the baseline in the peak, N_{hi}/N_{pk}, are useful for eliminating spurious noise-induced events. New statistics on uniqueness (pfrdev2), the passband power ratio (pfwsr), the red/blue cross-correlation coefficient outside the peak (rbcrossout), and the robust $\chi^2_{robust-out}/N_{dof}$ baseline statistic are useful in removing periodic and quasi-periodic variable stars. We have also more carefully characterized our main source of variable star background, the bumpers, in a magnitude–color magnification space (see Fig. 3). With the background of variable stars more effectively removed, we can both reduce our reliance on any "shape"-dependent criteria and lower the significance level of a detection. In § 4 we demonstrate the relative looseness of criteria set B over set A, as well as the decreased dependence on shape. However, one potential difficulty with criteria set B is its inability to discriminate against some types of variable stars, such as cataclysmic variables (CVs) and SNe, that might exhibit strongly asymmetric and/or chromatic light curves during the "event," but remain constant for long periods of time. Supernova removal is discussed separately in more detail below. See Table 2 for the definitions of the statistics and Table 3 for a complete list of the individual cuts used by selection criteria sets A and B.

3.2. Microlensing Candidates

We find 19 light curves that pass criteria set A and 29 light curves that pass criteria set B (before applying the SN cuts described below). All the light curves passing criteria set A also pass criteria set B. The 29 light curves are shown in Figure 4, and their microlensing fit parameters are listed in Table 4. Events that do not pass criteria set A are marked with an asterisk. Parameters for fits, including the possibility of blending with an unlensed star in the same seeing disk as the lensed star, are given in Table 5. The unblended fits are displayed as a thick line in Figure 4, used for all selection-criteria statistics except comparison with SN. Note that our events here are numbered as in A97 to avoid any possible ambiguity. Thus, the first event described here that was not described in A97 is event 13.[17]

Six of these 29 light curves (1a, 1b, 10a, 10b, 12a, and 12b) actually correspond to only three stars that occur in field overlap regions; the two light curves for each star are based on independent data and reductions. Two light curves are also of the same star (7a and 7b), but were not in field overlaps. Event 7 was bright enough and in a locally crowded enough region that some of the flux from the primary (7a) contaminated a secondary (7b) neighbor, causing a spurious detection. Event 7a passed both criteria sets A and B, while event 7b passed only criteria set B due to its low S/N. Thus, before SN removal there are 16 unique events found by the criteria set A, and 25 unique events found by the criteria set B.

3.3. Background

3.3.1. Bumpers

As noted in A97, a potential source of background to microlensing is a class of bright blue variables that we refer

---

[17] Finding charts for the events, as well as the full light curves, can be found at: http://wwwmacho.anu.edu.au/. A mirror site exists at http://wwwmacho.mcmaster.ca/, and the site for microlensing alerts is http://darkstar.astro.washington.edu.
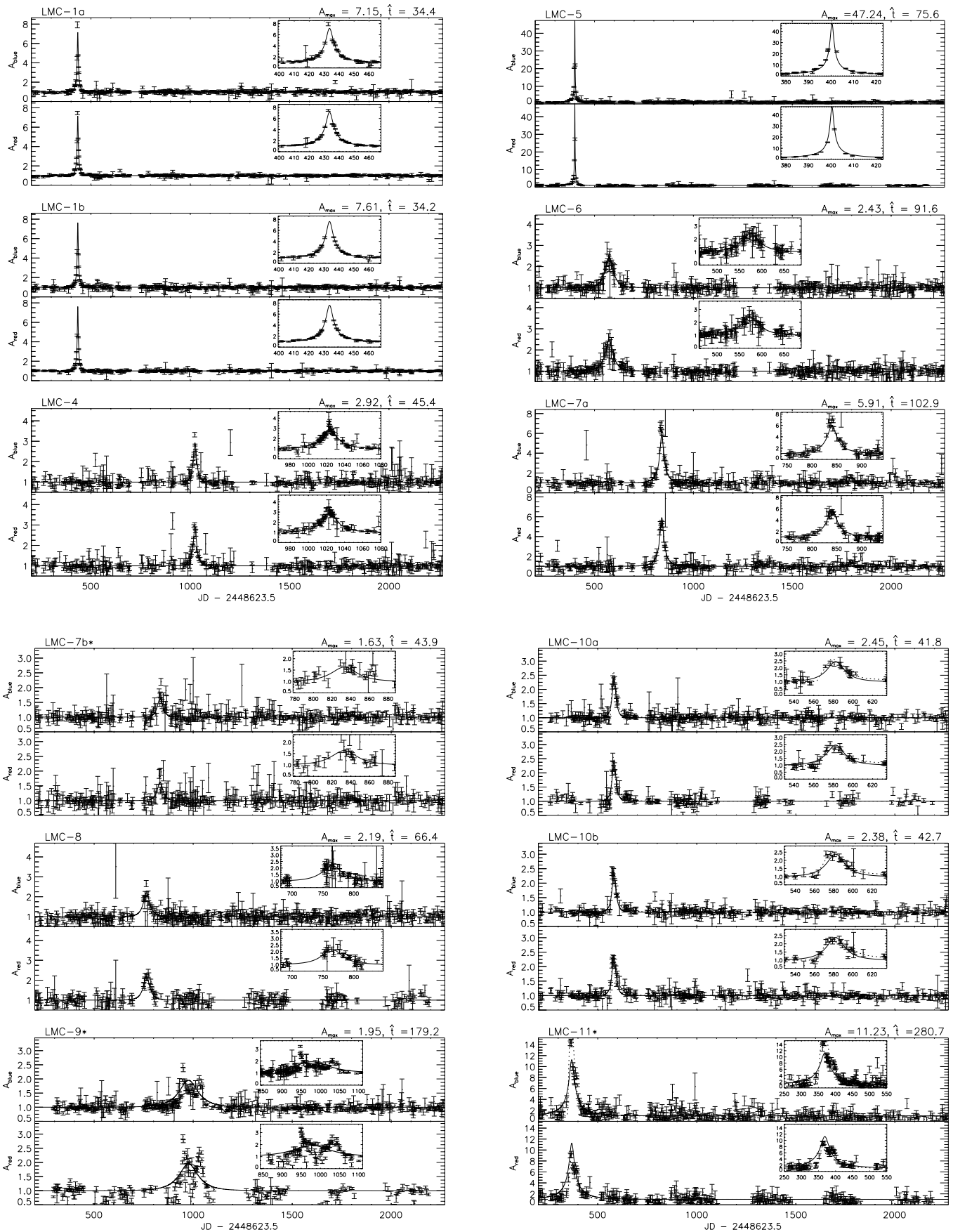
Fig. 4.—Light curves for the 29 candidates (25 stars) discussed in § 3.2. For each object, the top and bottom panels show blue and red passbands, respectively. Flux is in linear units with 1 σ estimated errors, normalized to the fitted unlensed brightness. Full light curves are shown with 2 day binning; insets of the event regions are unbinned. The thick line shows the fit to unblended microlensing (Table 5), except for probable SN, for which both the unblended fit (*solid line*) and SN Type Ia fit (*dashed line*) are shown.

LMC−12a $A_{max} = 7.32, \hat{t} = 137.4$
LMC−14 $A_{max} = 3.37, \hat{t} = 100.1$
LMC−12b $A_{max} = 7.31, \hat{t} = 170.5$
LMC−15 $A_{max} = 2.83, \hat{t} = 36.8$
LMC−13 $A_{max} = 2.36, \hat{t} = 100.1$
LMC−16∗ $A_{max} = 1.76, \hat{t} = 27.0$
LMC−17∗ $A_{max} = 1.85, \hat{t} = 24.1$
LMC−20∗ $A_{max} = 2.95, \hat{t} = 72.7$
LMC−18 $A_{max} = 1.54, \hat{t} = 74.2$
LMC−21 $A_{max} = 5.64, \hat{t} = 93.2$
LMC−19∗ $A_{max} = 1.41, \hat{t} = 16.3$
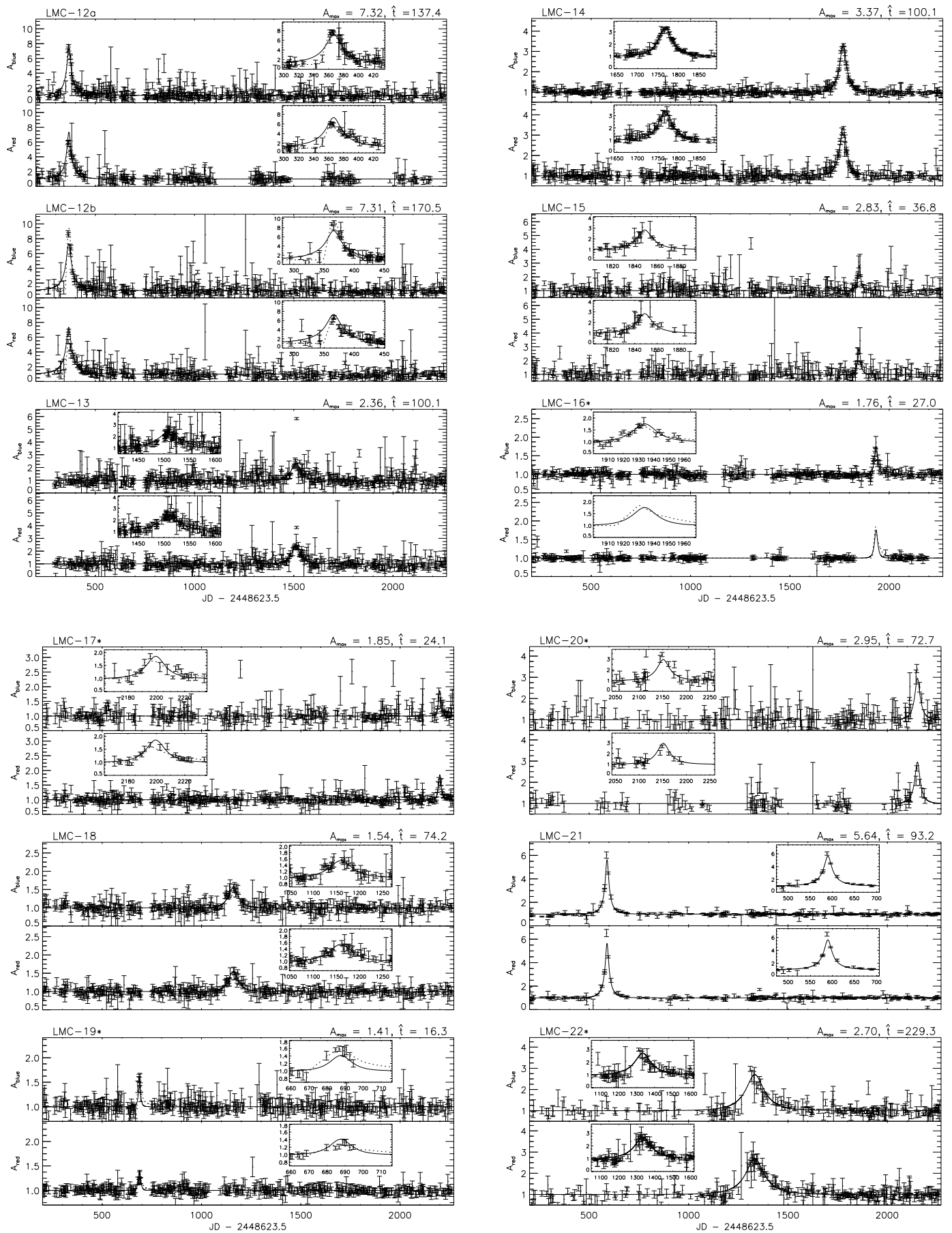LMC−22∗ $A_{max} = 2.70, \hat{t} = 229.3$

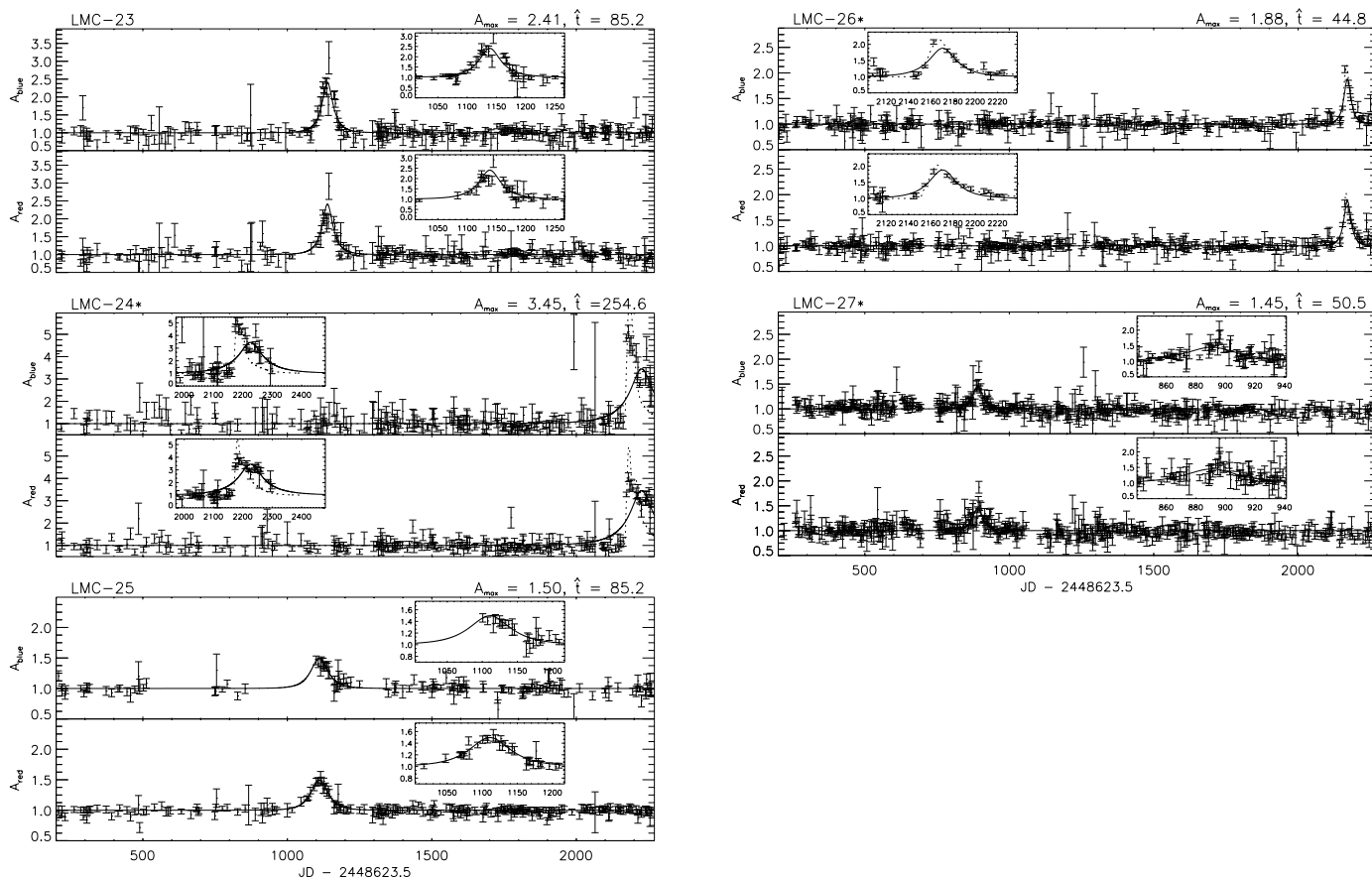JD − 2448623.5

FIG. 4.—*Continued*

289

Fig. 4.—*Continued*

to as "bumpers" (Cook et al. 1995). Although associated with Be stars, which are known to show periodic outbursts in our Galaxy, the true nature of these variable stars is still unknown. However, it is possible to eliminate bumpers as a serious source of background, since they can be well isolated in a 3 parameter space. For example, microlensing fits to bumpers seen in our data almost never return magnifications larger than 1.5, typically much less, as can be seen in Figure 2 (*open circles*).

One need not restrict selection to magnifications above 1.5, since the bumpers are also well isolated in the CMD, as illustrated in Figure 3. Here a typical CMD of the LMC is shown with a scattering of small dots. The 29 light curves that pass selection criteria set B are shown as filled circles and labeled. As in Figure 2, open circles indicate events that fail criteria set B's bumper cut. Filled squares indicate events that fail criteria set B's magnification cut, $A_{max} > 1.34$. The final cut on brightness, $V > 17$, and color-magnitude magnification (the bumper cut) are marked as solid lines for criteria set B (for comparison, the dotted line illustrates the bumper cut for criteria set A). If a potential event falls within the boxed region labeled "$A_{max} > 1.75$," then it must have a magnification greater then 1.75 to be included in the criteria set B set of events. We have visually inspected the ∼300 bumper candidate light curves and confirm that the vast majority of them show the slight asymmetry and other characteristics typical of the bumpers described in A96. In fact, due to the cut on uniqueness, these bumpers have only single bumps and evidently represent one-time-only bumpers or bumpers with interbump intervals longer than 5.7 yr.

3.3.2. *Supernovae*

Another serious source of potential contamination in microlensing surveys, which has not been given sufficient attention before, are SNe occurring in galaxies behind the LMC. These background SNe are picked up in the crowded fields, and their host galaxies are not always easy to identify in ground-based images. The fact that they occur only once and show a flat baseline before and after the event make SN interlopers a serious concern.

A first step in understanding this source of contamination is to estimate the number of SN we might see during the course of the experiment. Because of the recent interest in SNe Type Ia (SNe Ia) as standard candles, the rate of SNe (both Types I and II) occurring in field galaxies is now fairly well known. We use a typical rate of 0.5 SN yr^{-1} deg^{-2}, with peak magnitude brighter than $V \sim 20$ (Woods & Loeb 1998). The duration of the experiment is 5.7 yr and covers 13.5 deg^2, which suggests that we should have approximately 38 SNe in our data set. This does not include our SN detection efficiency and so is an overestimate. We expect our efficiency for detecting SNe to be on the order of 5%–15%, similar to that of detecting microlensing events (see § 4), due to the similar shapes of the corresponding light curves, implying that we are likely to see ∼2–6 SNe in the current data set.

If the density of galaxies behind the LMC is average, then the probability of finding a galaxy (that is close enough such that the survey might detect a SN within it) in proximity to a given star should be low. Therefore, a robust way of eliminating potential SN interlopers would be a search for a

TABLE 4

CANDIDATE MICROLENSING EVENTS

Event [a]	ID	R.A. (2000)	Decl. (2000)	V	$V - R$	t_{max}	$\hat{t}$	A_{max}	χ^2/N_{dof}
1a	2.5628.5917	05 14 44	−68 48 01	19.75	0.56	433.6	34.4	7.15	1.083
1b	79.5628.1547	05 14 44	−68 48 00	19.73	0.55	433.8	34.2	7.62	1.051
4	13.5961.1386	05 17 14	−70 46 58	20.25	0.14	1023.4	45.4	2.92	1.415
5	6.5845.1091	05 16 41	−70 29 18	21.15	0.76	400.4	75.6	47.28	1.512
6	7.7420.2571	05 26 13	−70 21 14	19.97	0.12	573.6	91.6	2.43	0.763
7a	10.3802.872	05 04 03	−69 33 18	20.87	0.32	840.0	102.9	5.91	1.398
*7b	10.3802.494	05 04 04	−69 33 18	19.85	0.18	832.9	43.9	1.63	1.046
8	77.7307.4800	05 25 09	−69 47 53	20.31	0.21	764.3	66.4	2.19	1.733
*9[b]	80.6468.2746	05 20 20	−69 15 11	19.58	0.27	976.4	179.2	1.95	6.579
10a[c]	1.3324.122	05 01 15	−69 07 33	19.60	0.23	582.2	41.8	2.45	1.455
10b[c]	18.3324.1765	05 01 16	−69 07 33	19.47	0.14	581.8	42.7	2.38	1.455
*11[c]	11.8746.130	05 34 21	−70 41 07	20.04	0.85	368.5	280.7	11.23	2.365
12a[c]	11.8622.1257	05 33 51	−70 50 57	21.34	0.25	366.6	137.4	7.32	1.238
12b[c]	14.8622.4762	05 33 51	−70 50 59	21.51	0.39	365.7	170.5	7.31	1.237
13	80.7080.5384	05 24 03	−68 49 12	21.02	0.26	1510.5	100.1	2.36	1.170
14	11.8871.2108	05 34 44	−70 25 07	19.37	0.01	1767.8	100.1	3.37	0.751
15	10.4162.3555	05 05 46	−69 43 51	21.03	0.14	1848.9	36.8	2.83	0.905
*16[c]	79.4655.4621	05 09 16	−69 08 15	18.71	0.56	1934.1	27.0	1.76	0.984
*17[c]	9.5362.408	05 13 35	−70 24 43	20.05	0.48	2199.5	24.1	1.85	1.059
18	15.10554.465	05 45 21	−71 09 11	19.55	0.35	1159.3	74.2	1.54	1.217
*19[c]	15.10669.178	05 46 18	−71 31 48	19.44	0.82	687.5	16.3	1.41	0.734
*20	17.2221.1574	04 54 19	−70 02 15	21.35	0.57	2151.2	72.7	2.95	1.298
21	17.2714.1058	04 57 14	−69 27 48	19.37	0.03	589.7	93.2	5.64	1.620
*22	22.5472.1126	05 14 32	−71 09 12	20.64	0.25	1333.2	229.3	2.70	1.277
23	23.4143.256	05 06 17	−70 58 47	20.27	0.31	1138.8	85.2	2.41	1.492
*24[c]	24.2862.1187	04 57 46	−67 41 08	20.63	0.49	2201.4	186.5	4.09	3.927
25	24.3583.2286	05 02 16	−68 00 52	19.04	0.48	1110.8	85.2	1.50	0.733
*26[c]	47.1764.464	04 51 11	−68 16 41	19.46	0.21	2170.6	44.8	1.88	1.305
*27	1.4289.1748	05 06 35	−69 20 48	19.24	0.07	890.6	50.5	1.45	1.239

NOTE.—The magnitudes and colors are fit baselines using the best available calibrations for each field as described in § 2. Time of peak magnification t_{max} is in JD −2,448,623.5 (1992 Jan 2).

[a] Events 1–12 appeared in A97. We number the current sample 1, 4, …, 27 to avoid any ambiguity with the previously published events. Events marked with an asterisk do not pass selection criteria set A.

[b] Event 9 is the binary microlensing event; the parameters here are those resulting from a single-lens fit, and are not strictly appropriate.

[c] Probable supernova.

background host galaxy in an image. If such a galaxy were found within a predetermined radius, the microlensing interpretation would be unlikely. Since the area covered by nearby galaxies is small, the correction to our experimental efficiency would be small. Unfortunately, our ground-based images have neither the resolution nor sufficiently low sky count to perform such a search with confidence. We do have *Hubble Space Telescope* (*HST*) observations of nine of our events (see Table 7 below), and these give us high confidence that six of them are not SNe, since there are no obvious background galaxies anywhere near these events. Two events for which we have an *HST* image (events 10 and 12) do show a fairly bright spiral galaxy within 5″. In retrospect, the host galaxy for event 10 shows up in our ground-based images, but could not have been recognized as a galaxy without additional data. This event was noticeably asymmetric in A97 and was classified as a marginal microlensing candidate. In calculating the optical depth, it was rejected from the 6 event sample, but included in the 8 event sample. Although the effect of its inclusion was small, increasing the reported optical depth of the 8 event sample by only 7%, its presence underscores the need to take potential SN contamination seriously.

Unfortunately, with an incomplete sample of *HST* images we are unable to follow the above prescription to reject SN interlopers completely. We have requested *HST*

time to observe the remaining events, and have examined the best available ground-based images for evidence of background galaxies. Fortunately, we can also use the shape of the light curve to help distinguish SNe from microlensing. Even though the light curves of SNe Type II are not well understood and exhibit a wide range of behaviors, SNe Ia have been studied in detail. Their light curves are very similar once distance, reddening, and a shape parameter are allowed for (Phillips 1993; Riess, Press, & Kirshner 1996). In addition, SNe Ia dominate the SN rate in flux-limited samples (Woods & Loeb 1998). Using the SN Ia templates of Riess et al. (1996) transformed to the MACHO photometric system, we have applied a 6 parameter SN Ia fit to all 29 light curves. The six free parameters of the fit are the baseline flux of the photometered object in red and blue passbands, f_{0R} and f_{0V}, respectively, and four parameters that describe the SN Ia light curve: the time of peak, t_{peak}, the distance modulus in the red (μ_R) and blue (μ_V) bands (fitted independently to account for the possibility of reddening), and a shape parameter, δ, that parameterizes how SNe Ia become longer in duration when intrinsically brighter. Empirically, we discovered that by allowing any acceptable value of δ, in many cases our best-fit SN shape was well outside the range of observed SNe (e.g., $\delta = 5$). This was especially true for high-quality microlensing events, for which the SN template provides a poor fit to the

TABLE 5
MICROLENSING FITS WITH BLENDING

Event[a]	t_{max}[b]	$\hat{t}$	A_{max}	f_{0V}	f_{0R}	f_V	f_R	χ^2/N_{dof}
1a	433.6	34.5	7.19	58.60	93.30	0.984	1.000	1.083
1b	433.7	34.7	7.83	47.23	77.38	0.972	0.982	1.052
4	1023.0	83.3	6.98	40.85	35.00	0.322	0.365	1.380
5	400.4	109.8	1.27×10^7	15.98	34.35	1.000	0.457	0.843
6	573.6	92.0	2.45	42.63	41.33	0.981	1.000	0.764
7a	840.1	112.6	6.87	23.12	25.51	1.000	0.748	1.328
*7b	833.2	46.5	1.71	61.37	56.25	1.000	0.761	1.042
8	764.3	66.4	2.19	38.45	32.52	1.000	1.000	1.735
*9[c]	979.5	143.4	...	79.37	83.30	0.260	0.170	1.755
10a[d]	582.1	43.6	2.56	74.38	71.49	1.000	0.871	1.451
10b[d]	582.0	128.8	10.12	79.99	67.05	0.163	0.160	1.447
*11[d]	367.7	436.9	20.96	31.24	93.80	0.998	0.366	1.965
12a[d]	367.1	213.5	13.41	13.09	15.59	0.604	0.440	1.184
12b[d]	367.0	1002.0	65.94	9.15	12.45	0.140	0.091	1.138
13	1510.0	222.7	6.95	17.79	17.64	0.219	0.260	1.158
14	1768.0	106.5	3.67	81.16	59.87	0.901	0.874	0.750
15	1849.0	41.9	3.48	20.11	16.88	0.776	0.735	0.906
*16[d]	1934.0	27.0	1.76	148.00	226.70	1.000	1.000	0.985
*17[d]	2200.0	24.3	1.88	42.44	61.96	1.000	0.960	1.060
18	1159.0	75.8	1.58	80.26	91.15	1.000	0.892	1.217
*19[d]	687.5	18.6	1.62	86.28	194.90	1.000	0.465	0.702
*20	2152.0	99.4	5.42	12.30	20.21	0.628	0.407	1.253
21	589.4	141.5	11.59	91.01	67.39	0.499	0.502	1.592
*22	1333.0	233.9	2.73	26.04	26.31	0.927	1.000	1.278
23	1139.0	88.9	2.61	39.25	41.98	1.000	0.801	1.452
*24[d]	2201.0	186.3	4.09	22.58	32.85	1.000	1.000	3.941
25	1111.0	85.3	1.51	112.50	156.40	0.924	1.000	0.734
*26[d]	2169.0	260.0	21.34	82.81	77.29	0.056	0.057	1.277
*27	895.0	3247.0	258.90	85.17	67.56	0.002	0.003	1.218

[a] Events marked with an asterisk do not pass selection criteria set A.

[b] Time of peak magnification t_{max} is in JD $-$ 2,448,623.5 (1992 Jan 2).

[c] For the binary microlensing event (9), the fit parameters are given for the binary lens fit (Alcock et al. 2000a). Not all of the these parameters are appropriate for this fit.

[d] Probable supernova.

shape of the light curve. We therefore limit our range in δ to be between -0.5 and 0.75, and note that for most of the events with poor SN fits, we find δ pegged at one of these values. The SN Ia fits are displayed as dashed lines for the events we categorize (see below) as SN in Figure 4, and the fit parameters for all 29 light curves are given in Table 6.

We summarize all the relevant available information for the 29 events in Table 7. Columns (2)–(4) compare the blended microlensing fits, χ^2_{ml}/N_{dof}, with the SN Ia fits, χ^2_{SN}/N_{dof}. A positive value of $\Delta\chi^2_{SN-ml}$ indicates a better fit to blended microlensing, while a negative value indicates a better fit to SN Ia. Inspection of Table 7 reveals 10 light curves (eight events) that are better fitted by SN Ia. As a consistency check, column (5) indicates the presence or absence of an obvious background galaxy within $\sim 10''-15''$, as determined using the best available image of the event (image source given). This background galaxy identification is subjective. Part of the problem is the severe crowding of the ground-based images used (MACHO or Cerro Tololo Inter-American Observatory [CTIO] images). In every case, where a galaxy is probably present the fit to a SN Ia template is preferred over the blended fit, giving us some assurance of the overall correctness of the procedure. We have no spectra to confirm the hypothesis that any of these eight events are, in fact, SNe Ia. However, given the fact that we should see 2–6 SNe in our survey, we feel that it is nevertheless prudent to eliminate these eight events as

potential interlopers. We thus implement as our final cut (on both selection criteria sets A and B) the requirement that the blended microlensing fit be preferred over the SN Ia fit, or $\Delta\chi^2_{SN-ml} > 0.0$. This eliminates events 10 and 12 from set A and events 10, 11, 12, 16, 17, 19, 24, and 26 from set B. Event 22, clearly not a SN Ia, is a special case and will be discussed later. The advantage of using this simple cut is that we can quantify the effect it has on the detection efficiency (see § 4). The effect is negligible, since less then 0.7% of artificial standard microlensing events are falsely rejected by this cut.

There are several important caveats to using the SN Ia fits to reject potential SN interlopers. First, both microlensing and SNe come in a variety of flavors. Although SNe Ia have well-defined light curves, other types of SNe are not so well behaved (e.g., Types Ib, Ic, IIp, Ill, etc.) and can come in a variety of durations and asymmetries. We note here that two of our SN interlopers (events 11 and 24) are likely to be SNe IIp, as judged by the plateau seen in both passbands about 25–50 days after maximum (never seen in both passbands R and V for SNe Ia). However, even these light curves are usually better fitted by SN Ia than blended microlensing, mostly due to the asymmetry that SN light curves typically exhibit.

Second, exotic microlensing, such as found in binary lenses, binary sources, or parallax events, could mimic the asymmetry of SNe Ia. There are several reasons why we

TABLE 6

SUPERNOVA TYPE Ia FITS

Event[a]	t_{max}[b]	μ_V	μ_R	δ	f_{0V}	f_{0R}	χ^2/N_{dof}
1a	431.1	37.44	36.82	0.75	57.86	92.39	3.946
1b	431.1	37.68	37.10	0.75	46.74	76.76	3.283
4	1020.0	38.11	37.98	0.75	40.75	34.88	1.617
5	397.1	36.94	36.76	0.75	15.21	34.57	4.187
6	566.4	39.49	38.89	−0.50	42.99	41.66	0.865
7a	837.1	37.44	37.50	0.70	23.14	25.60	1.385
*7b	830.1	38.50	38.69	0.75	61.39	56.26	1.058
8	758.1	39.63	39.19	−0.22	38.51	32.24	1.750
*9	952.1	39.02	38.10	−0.50	84.93	77.97	7.030
10a[c]	577.2	37.72	37.68	0.59	74.15	71.18	1.286
10b[c]	576.3	38.02	37.95	0.33	80.06	67.04	1.252
*11[c]	362.5	36.97	36.26	−0.42	36.47	98.99	1.871
12a[c]	363.2	38.45	38.24	0.14	13.33	15.74	1.101
12b[c]	363.9	38.66	38.45	0.11	9.59	12.77	1.128
13	1497.0	40.52	39.56	−0.50	18.41	18.15	1.287
14	1758.0	38.31	38.06	−0.50	82.35	60.47	1.754
15	1845.0	39.04	39.10	0.75	20.30	16.97	0.948
*16[c]	1930.0	37.78	36.91	0.75	148.00	226.60	0.976
*17[c]	2196.0	39.13	38.71	0.75	42.26	61.82	1.036
18	1147.0	39.49	38.92	−0.50	80.91	91.76	1.406
*19[c]	684.7	38.52	38.30	0.75	86.21	194.80	0.699
*20	2150.0	38.89	38.71	0.72	12.42	20.49	1.305
21	586.1	36.10	36.25	0.75	91.31	67.57	2.287
*22	1318.0	39.40	38.89	−0.50	26.83	27.32	1.797
23	1128.0	39.76	39.22	−0.50	39.98	42.12	1.855
*24[c]	2183.0	38.86	37.96	−0.50	23.56	34.24	3.544
25	1103.0	39.49	38.49	−0.50	113.00	157.80	1.243
*26[c]	2165.0	38.16	38.06	0.41	83.10	77.45	1.222
*27	892.9	38.64	38.62	0.75	86.24	68.44	1.302

[a] Events marked with an asterisk do not pass selection criteria set A.
[b] Time of peak magnification, t_{max}, is in JD − 2,448,623.5.
[c] Probable supernova.

believe that this is not a major problem: (1) event 9, a binary lens event, is better fitted by a single-lens microlensing light curve than a SN Ia light curve; (2) out of many microlensing events toward the Galactic bulge, less than 10% are of clearly exotic type (Alcock et al. 2000a),[18] and (3) exotic microlensing should show the "wrong" sign of asymmetry 50% of the time, and we have no examples of this among our events.

However, two events do stand out as potentially worrisome. Event 26 is better fitted by SN Ia, but does not show a clear background galaxy in our deepest CTIO 0.9 m images. It could be an example of exotic lensing. For the purposes of this paper, we reject this as a potential SN interloper, but we must await a better image before making any definitive conclusions regarding this event. Event 22 is our longest duration event and is clearly asymmetric to the eye. However, even with the clear asymmetry this event is better fitted with blended microlensing than with a SN Ia, mainly because SNe Ia are not observed to last this long. The asymmetry of this event is well fitted by microlensing parallax, which would be a natural explanation given the very long duration of this event. The fit parameters are: $u_{min} = 0.3$, $\hat{t} = 196$ days, $t_{max} = 1366.0$ days, $\tilde{v} = 78$ km s^{-1}, $\theta = 0.18$ radians, $\chi^2/dof = 1.15$; see Alcock et al. (1995a) for a definition of the parallax parameters. However, the source object for event 22 appears to be slightly extended in our

best 4 m CTIO image. In addition, we have spectra that show a number of emission lines that are characteristic of star-forming galaxies. The redshift is probably $z = 0.23$. Thus, it is quite uncertain whether event 22 is microlensing with parallax. It is also possible that event 22 belongs to a class of SNe ("slow" Type IIn) similar to SN 1988Z (Roscherr & Schaefer 1999; Schlegel 1990; Stathakis & Sadler 1991). Other possibilities certainly exist, but at present this event remains somewhat ambiguous. Therefore, in the spirit of our selection criteria, we reject event 22 from the exclusive set A and keep it in the inclusive set B. Since event 22 is our longest duration event and therefore contributes maximally to the optical depth, this is also the conservative approach to exploring the sensitivity of our results to the selection criteria.

3.4. How Many Events?

Here we briefly summarize the events that will constitute sets A and B. The main results of this paper rest on these two sets of candidate microlensing events.

Criteria A selected 19 light curves, corresponding to 16 unique events (events 1, 10, and 12 in field overlaps). Of these 16 unique events, two (events 10 and 12) are rejected as SN interlopers by the final SN cut, $\Delta\chi^2_{SN-ml} > 0.0$, and an unexplained event 22 is rejected in the spirit of criteria set A being exclusive. This leaves set A containing 13 events: 1, 4–8, 13–15, 18, 21, 23, and 25.

Criteria B selected 29 light curves, corresponding to 25 unique events (events 1, 10, and 12 in field overlaps and

TABLE 7

Supernova and Event Summary

Event[a] (1)	χ^2_{ml}/N_{dof} [b] (2)	χ^2_{SN}/N_{dof} (3)	$\Delta\chi^2_{SN-ml}$ (4)	Galaxy? (5)	Follow-Up (6)	Notes (7)
1a	1.083	3.946	6444	No (HST)	...	
1b	1.052	3.283	3685	No (HST)	...	
4	1.380	1.617	306	No (HST)	CTIO + spectroscopy	
5	0.843	4.187	4021	No (HST)	...	
6	0.764	0.865	173	No (CTIO)	...	
7a	1.328	1.385	71.0	No (HST)	...	
*7b	1.043	1.058	20.0	No (HST)	...	
8	1.735	1.751	28.0	No (HST)	...	
*9	6.269	7.029	1047	No (HST)	...	Binary microlensing
10a[c]	1.451	1.286	−163	Yes (HST)	...	
10b[c]	1.447	1.252	−226	Yes (HST)	...	
*11[c]	1.966	1.870	−117	Yes (CTIO)	...	
12a[c]	1.184	1.101	−113	Yes (HST)	...	
12b[c]	1.138	1.128	−12.0	Yes (HST)	...	
13	1.158	1.287	276	No (CTIO)	CTIO	
14	0.750	1.755	1724	No (HST)	CTIO	
15	0.906	0.948	45.6	No (CTIO)	CTIO	
*16[c]	0.985	0.976	−13.0	Yes (CTIO)	CTIO	
*17[c]	1.060	1.036	−31.0	Yes (CTIO)	CTIO	
18	1.217	1.406	274	No (CTIO)	...	
*19[c]	0.701	0.699	−3.1	Yes (CTIO)	...	
*20	1.253	1.305	23.9	No (CTIO)	...	
21	1.592	2.287	428	No (CTIO)	...	
*22	1.278	1.797	352	? (CTIO 4 m)	...	Microlensing parallax or rare SN?
23	1.452	1.855	263	No (MACHO)	...	
*24[c]	3.941	3.544	−218	Yes (MACHO)	...	
25	0.734	1.243	232	No (CTIO)	...	
*26[c]	1.278	1.222	−64.0	No (CTIO)	...	SN Type Ia or exotic microlensing?
*27	1.218	1.302	160	No (CTIO)	...	

NOTE.—This table summarizes the available information for each event, and a subjective "yes" or "no" determination of whether a background galaxy is present, along with the source of the image used in making the determination.

[a] Events marked with an asterisk do not pass selection criteria set A.
[b] Blended microlensing fits.
[c] Probably supernova.

event 7 duplicated via contamination). Of these 25 unique events, eight (events 10, 11, 12, 16, 17, 19, 24, and 26) are rejected as SN interlopers. Here we do not reject event 22, but leave it in the set as a potential exotic lensing event. As a result, set B contains 17 events: 1, 4–9, 13–15, 18, 20–23, 25, and 27.

4. DETECTION EFFICIENCY

The detection probability for individual events depends on many factors, e.g., the three event parameters A_{max}, $\hat{t}$, t_{max}, the unlensed stellar magnitude, and our observing strategy and weather conditions. Such a complicated dependence is most naturally determined using a Monte Carlo technique. We can simplify the dependence to some extent by averaging over the known distributions in A_{max}, t_{max}, the stellar magnitudes, and the known time-sampling and weather conditions, to derive our efficiency as a function only of event timescale, $\mathscr{E}(\hat{t})$.

We have computed our detection efficiency using a method similar to that outlined in A97, but with a number of improvements. A full discussion of the method, with detailed results, is given in Alcock et al. (2000b). Briefly, we generate simulated microlensing events with $\hat{t}$ logarithmically distributed in the range 1–2000 days over the slightly wider time interval, JD − 2,448,623.5 = 190.0 to 2277.0, and add these simulated events into the extended time span

of observations. A large database of artificial star tests is used to simulate the effects of blending. A number of systematic photometric effects, including the response of flux, error bars, and the photometric flags outlined in § 2, are also included. The Monte Carlo procedure takes into account the actual spacing and error bars of the observations, so any variations in sampling frequency, weather, seeing, etc., between the A97 data set and the current data set are automatically accounted for.

One of the primary shortcomings of the efficiency analysis presented in A97[19] was a lack of faint "stars" in the artificial star tests, which are used to add simulated events. In the current analysis, a large number of faint stars down to $V \sim 24.5$ are used. This is 2.5 mag fainter than in A97. It is also 2.5 mag fainter than our faintest detected objects. The present analysis also makes use of a much larger database of artificial stars ($\times$ 5) sampled over a larger ($\times$ 15) and more fairly distributed set of observing conditions (stellar density, seeing, and sky). Another major improvement, not fully recognized as a major source of uncertainty in A97, is a normalization of our fields to the

[19] We consider here only the "photometric" efficiency defined in A97. The "sampling" efficiency also described in A97 is of little value for the discussion of this paper. Sampling efficiencies for the present analysis can be found in Alcock et al. (2000b).

underlying luminosity function. A central issue in efficiency determination is the distinction between "objects" and stars. Objects are flux concentrations identified by the photometry code as stellar-like objects. Each object is typically a blend of many underlying LMC stars, any one of which can undergo microlensing, and it is important to identify the correct density of underlying LMC stars in each of our fields.

The present efficiency is based on all stars in our fields, even those not uniquely identified because of S/N or crowding effects. These are accounted for by integrating the detection efficiency per star over the true underlying luminosity function (LF) in the LMC. Our LF in the LMC is derived from a combination of ground-based MACHO photometry (for stars with $V < 20$) and multiple *HST* WFPC2 fields in the LMC bar (for stars with $V > 20$) and is described in Alcock et al. (2000b, 1999b). The shape of the LF appears universal in most of our fields and is well constrained for $V < 22$. Moreover, any reasonable deviation from the adopted shape down to $V \sim 24$ has little effect on our efficiency (Alcock et al. 2000b).

An important and yet uncertain factor is the normalization of the LF in each of our fields, which determines our effective sensitivity or exposure in star-years. Because our exposure in *object-years* is well known, and the efficiency should converge at some magnitude (as fainter stars contribute less and less), we have chosen to factor this normalization into the efficiency. Thus, our efficiency is properly defined as $\mathscr{E}(\hat{t}) = [(S/O)(V < 24)]\mathscr{E}_{stars}(V < 24, \hat{t})$, where $\mathscr{E}_{stars}(V < 24, \hat{t})$ is the efficiency per star integrated to $V = 24$ and $[(S/O)(V < 24)]$ is the normalization, or the number of stars per object (defined as the ratio of the true number of stars with $V < 24$ to the number of SoDoPHOT objects). Note that $\hat{t}$ in all of these expressions is the $\hat{t}$ input into the Monte Carlo, which is not actually available in real data. For observed events, our best estimate of this $\hat{t}$ is the statistically corrected fit $\hat{t}$ listed in Table 8 (see below). The value of $[(S/O)(V < 24)]$ is 10.84 ± 2.4 stars per object and represents a weighted average over all 30 fields. The limiting magnitude $V = 24$ was chosen because the efficiency for durations $\hat{t} < 300$ days converges. The efficiency for longer durations does not converge by $V = 24$, and thus these are likely to be underestimated, with the underestimation becoming worse for longer duration events. The exact point and speed of convergence is sensitive to the assumed shape of the LF and the cuts used, with criteria set A converging more rapidly (see Alcock et al. 2000b). Since none of our 13–17 events have durations longer than 300 days, our efficiency determination for them is sound. The uncertainty in the efficiency is dominated by the uncertainty in the normalization, which we estimate to be $\approx 20\%$ (see Alcock et al. 2000b for a more detailed error budget).

Efficiency results are shown in Figure 5. Selection criteria set A is shown as a solid line, and criteria set B as a dotted line. Also shown, for comparison, are the efficiencies presented in A96 (*long-dashed line*) and A97 (*short-dashed line*). Note that the efficiencies presented here have been scaled by a normalization term that accounts for the increased exposure due to all stars in our fields, down to $V = 24$ (as described above). Strictly speaking, the efficiency defined in this manner is not constrained to lie below 1, although in practice it always does. This efficiency is defined relative to an "exposure" of $E = 6.12 \times 10^7$ object-years, which arises as follows: there are 11.9 million light curves in our total

TABLE 8
MICROLENSING EVENTS USED, EFFICIENCY-CORRECTED $\hat{t}$, AND SINGLE-EVENT OPTICAL DEPTHS

Event[a]	$\hat{t}$	$\hat{t}_{st}(A)$	$\hat{t}_{st}(B)$	$\tau_1/10^{-9}(A)$	$\tau_1/10^{-9}(B)$
1	34.2	41.9	44.5	5.0	3.8
4	45.4	55.5	59.0	5.9	4.5
5	75.6	92.4	98.1	8.3	6.7
6	91.6	112.0	118.9	9.7	7.9
7	102.9	125.8	133.6	10.7	8.7
8	66.4	81.1	86.2	7.5	6.1
*9	143.4	...	143.4	...	9.3
13	100.1	122.4	130.0	10.5	8.5
14	100.1	122.4	130.0	10.5	8.5
15	36.8	45.0	47.7	5.2	4.0
18	74.2	90.7	96.4	8.2	6.6
*20	72.7	...	94.3	...	6.5
21	93.2	113.9	121.0	9.9	8.0
*22	229.3	...	297.8	...	20.0
23	85.2	104.2	110.7	9.1	7.4
25	85.2	104.2	110.7	9.1	7.4
*27	50.5	...	65.6	...	4.9

NOTE.—The quantity $\hat{t}_{st}$ is the average actual event timescale for events in our Monte Carlo calculations that are detected with an unblended fit timescale of $\hat{t}$. For the binary event 9, the blended binary fit $\hat{t}$ value is used. The quantity τ_1 is the contribution of each event to the total microlensing optical depth, computed using eq. (2). Columns are marked (A) or (B) to indicate which selection criteria were used in the efficiencies.

[a] Events marked with an asterisk do not pass selection criteria set A.

sample, and 20% occur in field overlaps. The relevant time span is the 2087 day interval over which we add the simulated events; thus, the exposure is 10.7×10^6 objects $\times$ 2087 days $= 6.12 \times 10^7$ object-years. This expo-
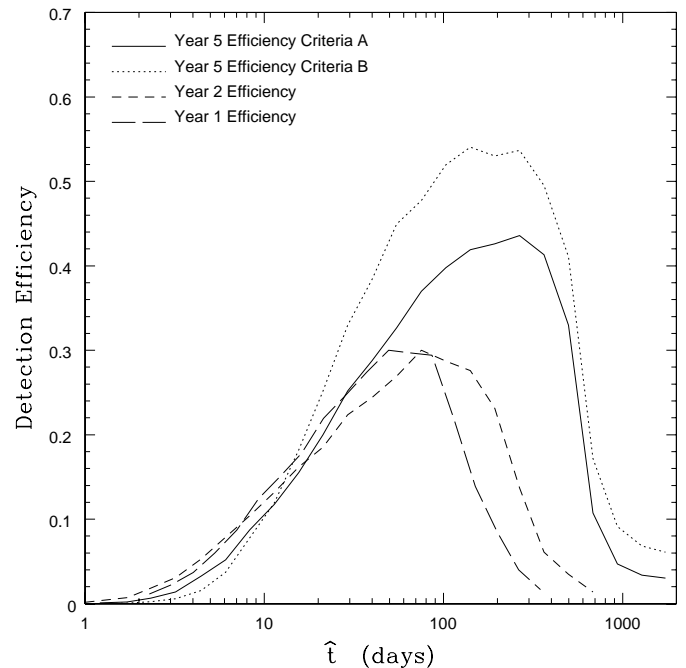

FIG. 5.—Microlensing detection efficiency (normalized to $u_{min} < 1$) for the 5.7 yr MACHO data, as a function of event timescale $\hat{t}$. The solid line shows the "photometric" efficiency computed for cut A, and the dotted line for cut B, as described in § 4. For comparison, the corresponding curves from year 1 (A96; *short-dashed line*) and year 2 (A97; *long-dashed line*) are also shown. See the electronic edition of the Journal for a color version of this figure.

sure is 3.4 times larger than in A97. Note that the number of stars in field overlaps has increased from 12% in A97, due to additional fields and a more careful calculation of the field overlap size.

The most striking difference between the previous two data sets (A96 and A97) and the current set is the much higher efficiency at long durations. Most of this difference is a reflection of having 5.7 yr of data instead of 2.1 yr. Explicit cuts in A97 were made that removed any events with $\hat{t} > 300$ days, while the current cuts both use $\hat{t} > 600$ days. However, some of the difference also lies in a quirk of the 2 yr data set. In A97, six of the densest fields had their light curves roughly cut in half, due to an early generation of templates used to reduce the photometry for these fields. The effect of this was a lowered efficiency in A97 for events with durations longer than $\hat{t} \sim 100$ days (mainly due to the required 40 baseline points in the "halved" light curves). The problem did not exist in the 1 yr data; thus the rather similar behavior of 1 and 2 yr data at large $\hat{t}$, even though the latter had twice the coverage. As described in § 2, the photometry for these six fields has been rerun with the new generation of templates, and the light curves merged onto a common photometric system.

The relative looseness of selection criteria set B over criteria set A discussed in § 3.1 (i.e., 17 versus 13 events) is well illustrated in Figure 5. Only for short durations, $\hat{t} < 10$ days, is criteria set A more efficient, due to criteria set B's larger number of required high points (≥ 10) as compared to criteria set A (≥ 7). Less than half of the difference in efficiency between criteria set A and set B is explained by the different $A_{\max}$ cuts; given $A_{\max}$ cuts of 1.49 and 1.34 for criteria sets A and B, respectively, we naively expect criteria set B to recover 17% more events. In fact, only event 27 (7%) would have been missed had criteria set B's $A_{\max}$ cut been increased to 1.49. The remainder of the difference lies primarily in the effect of two cuts. Many of the events that failed criteria set A did so because they failed either the cut in $\Delta\chi^2/(\chi^2_{\mathrm{peak}}/N_{\mathrm{dof}})$ or the cut in $\chi^2_{\mathrm{ml\text{-}out}}/N_{\mathrm{dof}}$. Both of these cuts have been tightened from their 2 yr values. Using simulated microlensing events, we find that tightening these two cuts lessens our sensitivity to moderately or strongly blended events, and that tightening the $\Delta\chi^2/(\chi^2_{\mathrm{peak}}/N_{\mathrm{dof}})$ cut decreases our sensitivity to exotic microlensing and other asymmetric light curves, such as SNe. For example, the slightly asymmetric event 26 did not pass criteria set A because of the cut $\Delta\chi^2/(\chi^2_{\mathrm{peak}}/N_{\mathrm{dof}}) > 350$. As a result, set A has fewer events removed by the SN cut.

In Alcock et al. (2000b), we describe in detail a robust way of statistically correcting for the $\hat{t}$ bias induced by blending. Briefly, this method is an integration over the LF of the median $\hat{t}$ bias induced by blending in our sample of Monte Carlo events. As a check that this method gives a truly unbiased optical depth estimate, we ran a series of secondary Monte Carlo simulations that make use of this correction and a number of Galactic halo models. The statistical correction, although it blurs the individual events together, does a satisfactory job of reproducing an unbiased optical depth.

The primary shortcoming of the present efficiency analysis is that all simulated events are assumed to be "normal" microlensing events with a single lens, a point source, and constant velocities. This assumption is used in the present analysis for simplicity and because of our highly uncertain knowledge of the distribution of exotic lensing

events. A careful study using selection criteria much looser than criteria sets A and B has convinced us that it is unlikely that we have missed any exotic lensing events in the present data set. The primary concern is what effect the addition of exotic lensing might have on our detection efficiency (in particular because of binary lensing events). Although this is as yet uncertain, it is probably a small effect, due to the small number of exotic lensing events seen so far and the fact that criteria set B does not find any exotic lensing events.

5. EVENT DISTRIBUTIONS

There are a number of statistical tests that can be performed on microlensing event distributions to test the hypothesis that events are gravitational microlensing, or to test hypotheses regarding the lens population. As the sample of events becomes larger, these tests become important discrimination tools.

5.1. Impact Parameters

An important model-independent test of the hypothesis that we have observed gravitational microlensing is to compare the distribution of peak magnifications to the theoretical prediction. It is convenient to switch variables from the maximum magnification ($A_{\max}$) to the minimum distance of approach between the MACHO and the line of sight, in units of the Einstein radius, $u_{\min} = b/r_E$. Events should be uniformly distributed in $u_{\min}$; this distribution is then modified by the experimental detection probability, which is typically higher for small $u_{\min}$ (Alcock et al. 2000b). The observed and predicted distributions for our LMC events for both selection criteria are shown in Figure 6. A Kolmogorov-Smirnov (KS) test shows a probability of
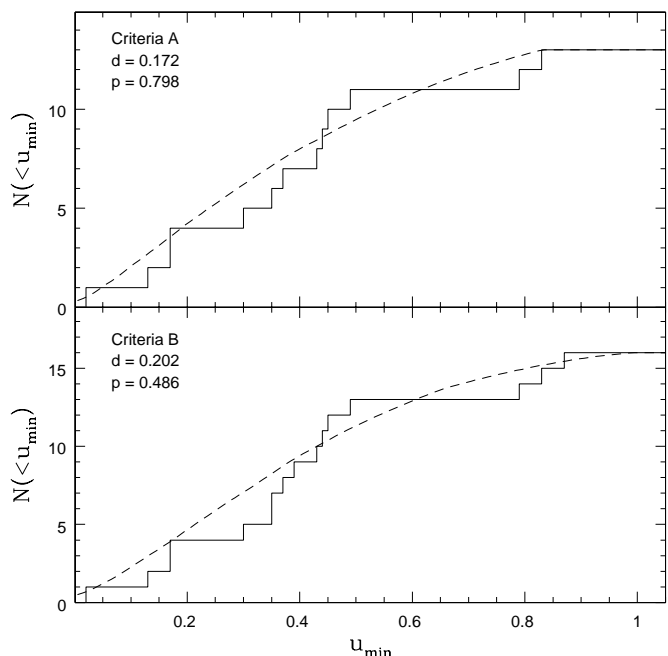

FIG. 6.—Cumulative distribution in $u_{\min}$ for set A (*top*) and set B, excluding the binary event 9 (*bottom*). The expected distribution is shown by the dashed line: a uniform distribution modified by our efficiency. The results of KS tests comparing the observed and expected distributions are also shown. See the electronic edition of the Journal for a color version of this figure.

79.8% of getting a KS deviation worse than the observed value of 0.172 for criteria set A by chance, and a probability of 48.6% of getting one worse than 0.202 for criteria set B. The binary event 9 is excluded from this comparison. We conclude that the distribution of events in u_{min} is consistent with the microlensing interpretation.

The u_{min} distribution and the high-magnification events can be used to lend support to the microlensing interpretation of our lower magnification events. Our high-magnification events are striking, and are clearly separated from the background in Figure 2. If these high-magnification events are accepted as microlensing, then there must exist many more microlensing events with smaller peak magnifications. Figure 6 shows that we find these in just the right proportion.

5.2. The Color-Magnitude Distribution

The gravitational microlens does not distinguish between types of stars, so naively one would expect microlensing to occur uniformly on every type of source star. However, both selection criteria sets A and B employ various S/N cuts that bias us against detecting microlensing events on faint stars. In addition, the measured baseline flux of an event may be significantly larger because of the blending of nonlensed flux, and it is not always possible to accurately determine the amount of blending. That is, the blending fits in Table 5 may not be reliable, since there is considerable fit parameter degeneracy between A_{max} and the blend fraction. Thus, detected microlensing candidates, while occurring on many types of source stars, may not follow the observed distribution of stars (or rather objects) exactly.

Figure 7 shows a CMD with each of the 17 microlensing candidates, along with all the closest 200 stars around each candidate. Most of the events lie along the faint main
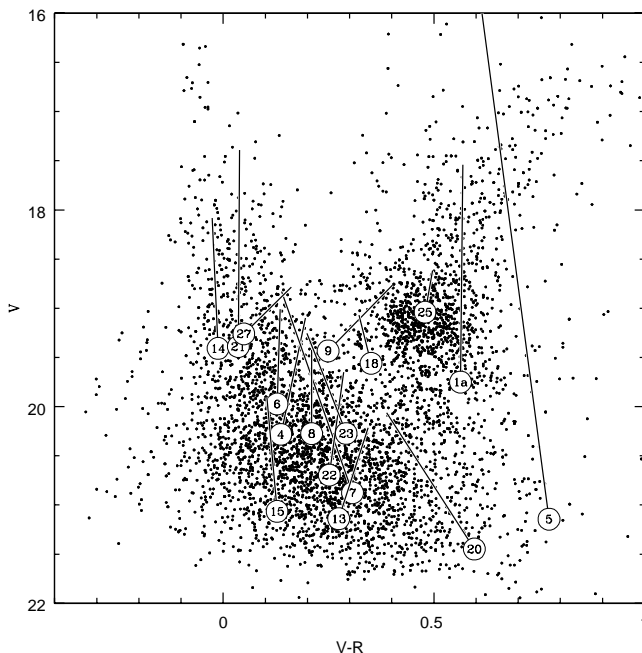
FIG. 7.—Candidate microlensing events. The open circles indicate the position in the CMD of the blended MACHO object. The lines extend to the peak brightness of the event. The points correspond to the 200 MACHO objects nearest each event. The best available calibrations for each field described in § 2 have been used for this figure.

sequence, where most of the observed LMC stars reside. Event 5 is quite red for its brightness and could represent a foreground population of bright M dwarf lenses, as noted in A97, but as a whole the distribution in the CMD is quite representative. The distribution of events is not clustered in luminosity or the CMD and is consistent with the microlensing interpretation.

5.3. Spatial Distribution

For microlensing by MACHOs smoothly distributed in the Galactic halo, or stellar lensing by stars in the Milky Way thin disk, thick disk, or spheroid, we expect the detected events to be distributed across our fields in proportion to the local exposure. An extended LMC halo population could also form a smooth distribution, with a small asymmetry due the inclination of the LMC disk, but differentiation of this from a Milky Way halo is probably impossible without many more events (Gould 1993). In contrast, models in which LMC disk and bar stars dominate the lensing population predict that the lensing events will be concentrated within the LMC (A97; Aubourg et al. 1999; Salati et al. 1999; Gyuk, Dalal, & Griest 2000), but see also Alves & Nelson (1999), who argue that a flared disk could widen this distribution to some extent.

Figure 1 indicates that the detected events are apparently spread evenly across our 30 fields. To quantify this impression we perform two simple tests. For criteria sets A and B, we computed a concentration parameter, $\tilde{\theta}$, as described in Gyuk et al. (2000). This parameter is a mean spatial separation between all combinations of events. For our two selection criteria, we find $\tilde{\theta}_A = 1°.94 \pm 0°.23$ and $\tilde{\theta}_B = 1°.86 \pm 0°.23$, where the error bars have been estimated using the observed number of events and the models of Gyuk et al. (G. Gyuk 1999, private communication). These numbers should be compared with predictions from the various models of LMC self-lensing. Gyuk et al. (2000) find $\tilde{\theta} = 1°.3 \pm 0°.2$ over the MACHO 30 fields for all their LMC disk + bar self-lensing models, and $\tilde{\theta} = 1°.85 \pm 0°.15$ for LMC disk + bar + halo and Galactic halo models. Thus, by this measure our event distribution is inconsistent with their most favored LMC disk + bar self-lensing at the $\sim 2\,\sigma$ level, but is consistent with an extended lens population, such as is expected for a Galactic or LMC halo population.

Our second test is illustrated in Figure 8, where the cumulative distribution in spatial distances on the sky, as measured from the optical center of the bar ($\alpha = 5^h24^m$, $\delta = -69°48'$), is plotted. Also shown are two predictions based on the models of Gyuk et al. (2000): the dashed line shows the predicted distribution for uniform lensing (LMC disk + bar + halo) over the face of the LMC, convolved with our detection efficiency per field (Alcock et al. 2000b), and the dotted line shows the favored LMC disk + bar self-lensing model, also convolved with our detection efficiency per field. For criteria set A, a KS test yields a probability of 7.3% of getting a KS deviation worse than the observed value of 0.342 for the disk + bar model. For the disk + bar + halo model, there is a probability of 59.5% of getting a KS deviation worse than the observed value of 0.204. For criteria set B, a KS test yields a probability of 2.4% of getting a KS deviation worse than the observed value of 0.349 for the disk + bar model, and for the disk + bar + halo model there is a probability of 34.1% of getting a KS deviation worse than the observed value of 0.220. We note that these results are dependent on a direct
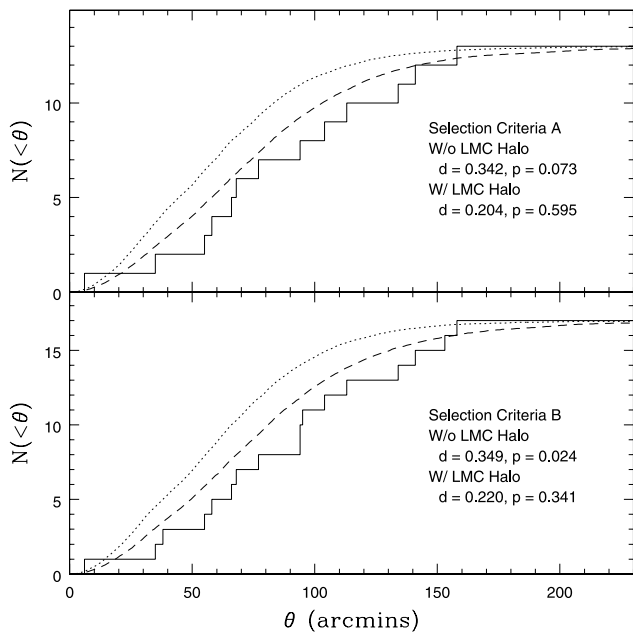
FIG. 8.—Cumulative spatial distribution on the sky as measured from the optical center of the bar ($\alpha = 5^{\rm h}24^{\rm m}$, $\delta = -69°48'$) for set A (*top*) and set B (*bottom*). The predictions of Gyuk et al. (2000) for the case of stellar LMC disk + bar self-lensing only (*dotted line*) and LMC disk + bar + halo self-lensing (*dashed line*) are also shown. The models of Gyuk et al. (2000) have been folded into our efficiency per field for each of the 30 fields reported on here. The results of KS tests comparing the observed and expected distributions are also shown. See the electronic edition of the Journal for a color version of this figure.

comparison to the 30 fields used in this analysis, and that the LMC disk + bar self-lensing predictions are inconsistent with the data at the 93% confidence level.

6. IMPLICATIONS

We start with the implied microlensing optical depth, which is compared with the optical depth expected from known populations of stars along the line of sight to the LMC. We then discuss our likelihood estimate of the microlensing rate, MACHO masses, and optical depth for both the dark halo and known stellar populations.

6.1. Optical Depth Estimates

The simplest measurable quantity in a gravitational microlensing experiment is the microlensing optical depth, τ, which is defined to be the instantaneous probability that a random star is magnified by a lens by more than a factor of 1.34. This probability depends only on the density profile of lenses, not on their masses or velocities. Experimentally, one can obtain an estimate of the optical depth as

$$\tau_{\rm meas} = \frac{1}{E} \frac{\pi}{4} \sum_i \frac{\hat{t}_i}{\mathscr{E}(\hat{t}_i)} , \qquad (1)$$

where $E = 6.12 \times 10^7$ object-years is the total exposure, $\hat{t}_i$ is the Einstein ring diameter crossing time of the ith event, and $\mathscr{E}(\hat{t}_i)$ is its detection efficiency. Here and below, we use the statistically corrected values of the blended durations, $\hat{t}_{\rm st}$ (Table 8). These take into account the fact that our typical star is blended, and so the fit $\hat{t}$ is typically underestimated. This statistical correction depends on the selection criteria

used and is described more fully in § 4. It is also convenient to define the function

$$\tau_1(\hat{t}) = \frac{1}{E} \frac{\pi}{4} \frac{\hat{t}}{\mathscr{E}(\hat{t})} , \qquad (2)$$

which is the contribution to $\tau_{\rm meas}$ from a single observed event with timescale $\hat{t}$. The τ_1 values for each of our events are also listed in Table 8 for both selection criteria.

Using the criteria set A set of 13 events, we find (Tables 9 and 10) an optical depth for events with durations $2 < \hat{t} < 400$ days of $\tau_2^{400} = 1.1 + 0.4 - 0.3 \times 10^{-7}$. With the criteria set B set of 17 events, we find $\tau_2^{400} = 1.3 + 0.4 - 0.3 \times 10^{-7}$. This is to be compared with $\tau = 4.7 \times 10^{-7}$ for a typical dark halo consisting entirely of MACHOs, and with predicted $\tau_{\rm stars} = 0.24 \times 10^{-7}$–$0.36 \times 10^{-7}$ from known stellar populations (from Table 12 below). Subtracting the stellar lensing background from our observed optical depth, we find that the observed excess is about 15%–25% of the predicted microlensing optical depth for a typical all-MACHO halo of equation (4) below.

This optical depth estimate has the virtue of simplicity; however, since the events are "weighted" $\propto \tau_1$, it is difficult to assign meaningful confidence intervals to τ without assuming some particular $\hat{t}$ distribution (Han & Gould 1995). This is illustrated in Figure 9, which shows the contribution to the sum in equation (1) from events in various bins of $\hat{t}$. In comparison with A97, we note that while the contributions become large at large $\hat{t}$, they are substantially smaller in the 100–300 day range, due to the increased baseline and looser cut of $\hat{t} < 600$ days. The large contribution at long $\hat{t}$ implies that the overall uncertainty in τ is greater than simple Poisson statistics based on 13 or 17 events. However, this uncertainty has continued to decrease as the experiment has progressed. For example, in A97 we estimated that if we expected to observe on average 1 additional event with $\hat{t} \sim 300$ days (but happened to observe no such event), the real τ would have been a factor of 2 higher, and we were not able to exclude such a possibility with any confidence. The equivalent situation with the current data set is less dangerous, since such a missed event would result in a real τ only about 20% higher. However, our optical depth estimate is valid only for a specific mass or timescale interval. The likelihood method of § 6.2 gives another way of estimating the optical depth and its confidence interval.

TABLE 9

TOTAL MODEL-INDEPENDENT OPTICAL DEPTHS

Criteria and $\hat{t}$	Number of events	Measured $\tau \times 10^7$	$\tilde{\theta}$ (deg)
A $\hat{t}$ statistical	13	$1.10^{+0.4}_{-0.3}$	1.94 ± 0.29
A $\hat{t}$ blended fit	13	$1.14^{+0.4}_{-0.3}$	...
A $\hat{t}$ unblended fit	13	0.94	...
B $\hat{t}$ statistical	17	$1.29^{+0.4}_{-0.3}$	1.86 ± 0.23
B $\hat{t}$ blended fit	17	$1.24^{+0.4}_{-0.3}$	...
B $\hat{t}$ unblended fit	17	1.08	...

NOTE.—The table entries show the microlensing optical depth τ in units of 10^{-7}, for the two selection criteria sets A and B using different $\hat{t}$ corrections (due to blending). The quoted errors are 1 σ standard errors computed as described in A97. The statistical $\hat{t}$ correction is preferred because it is unbiased. The "no $\hat{t}$ correction" values are given for comparison only. The column labeled $\tilde{\theta}$ gives the concentration parameter discussed in § 5.3.

TABLE 10

OPTICAL DEPTH CONFIDENCE INTERVALS

	NUMBER	$\tau \times 10^{-7}$ for Confidence Level:						
SELECTION CRITERIA	OF EVENTS	0.025	0.05	0.16	Measured	0.84	0.95	0.975
A	13	0.60	0.67	0.83	1.10	1.47	1.73	1.86
B	17	0.73	0.81	0.99	1.29	1.69	1.97	2.10
AB average.......	...	0.67	0.74	0.91	1.20	1.58	1.85	1.98
A likelihood	13	0.40	0.46	0.62	0.92	1.32	1.61	1.76
B likelihood	17	0.52	0.58	0.74	1.05	1.44	1.73	1.87

NOTE.—The table entries show limits at various confidence levels on the microlensing optical depth τ in units of 10^{-7} for different choices of selection criteria and different calculational methods. Rows marked A and B are model-independent values found using the Monte Carlo method described in A97. The center row is the average of the model-independent A and B calculations. The rows marked "likelihood" are background-subtracted (that is, for halo microlensing only) and depend on the model of the Galaxy and LMC used, in this case model "S" with a dark LMC halo included, as described in § 6.2.3.

6.1.1. Optical Depth Cut Dependence

Figures 10 and 11 show the dependence of the measured optical depth on the u_{min} and $\Delta\chi^2/(\chi^2_{ml}/N_{dof})$ cuts. The heavy curves indicate τ_{meas} for set A, while the lighter curves give τ_{meas} for set B. For the binary event, we have assigned a u_{min}

TABLE 11

OPTICAL DEPTH ERROR BUDGET

Cause	Size ($\tau/10^{-7}$)	Relative Size
Poisson	0.4	30%
Exposure/normalization of S/O......	0.25	20%
Selection Criteria	0.25	20%
$\hat{t}$ bias	0.05	3%
Binary star sources	?	?
Exotic lensing	?	?

value of 0.573, which is the value obtained for the single-lens fit.

Figures 10 and 11 clearly indicate that our optical depth results are not very sensitive to our cut values. The τ_{meas} values generally do not vary by more then the 1 σ statistical error bars for u_{min} and $\Delta\chi^2/(\chi^2_{ml}/N_{dof})$ cuts in the ranges $0.2 \leq u_{min} \leq 1.0$ and $300 \leq \Delta\chi^2/(\chi^2_{ml}/N_{dof}) \leq 5000$. We note that the largest single contribution is from event 22, which was included in set B and excluded from set A.

6.1.2. Comparison of A97 with the Present Analysis

Why is our new value of the optical depth a factor of 2 smaller than the value reported in A97? The reasons are manifold and somewhat difficult to separate out completely. By far the largest effect can be classified as Poissonian in nature. We list the causes in order of decreasing effect on the optical depth.

Inspection of Figure 4 reveals that a disproportionate number of our "high-quality" events were observed in the
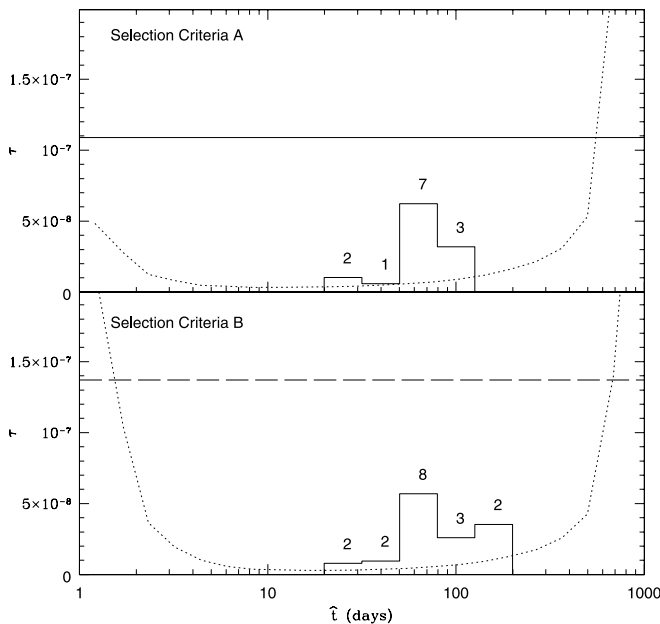

FIG. 9.—Contribution to the optical depth of eq. (1) from events binned in timescale for selection criteria set A (top) and set B (bottom). The histogram shows the observed values from the samples, with the number of events shown in each bin. The dotted curve shows the contribution to τ that would arise from a single observed event with timescale $\hat{t}$. The dashed line shows the total optical depth. See the electronic edition of the Journal for a color version of this figure.
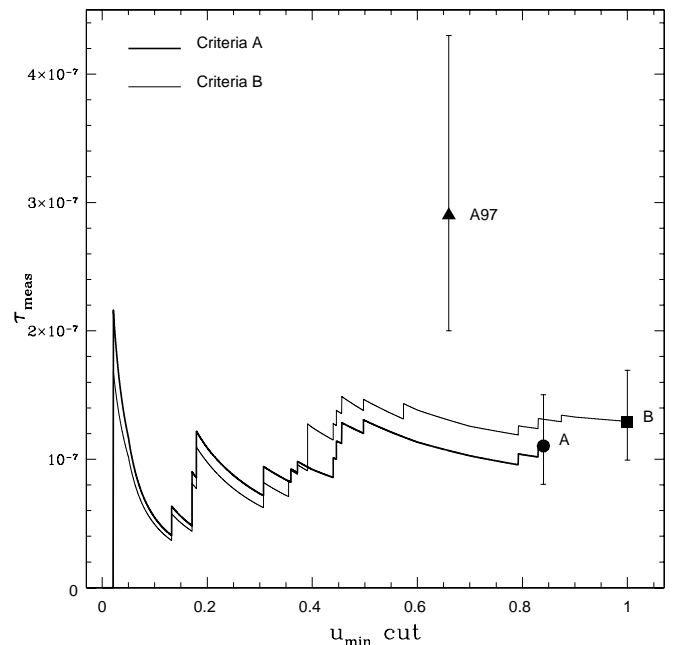

FIG. 10.—Measured microlensing optical depth, plotted as a function of the u_{min} cut for selection criteria set A (thick line) and set B (thin line). Our selected cuts for criteria sets A and B are marked with large filled circles with 1 σ error bars. The optical depth reported in A97 is also shown. See the electronic edition of the Journal for a color version of this figure.
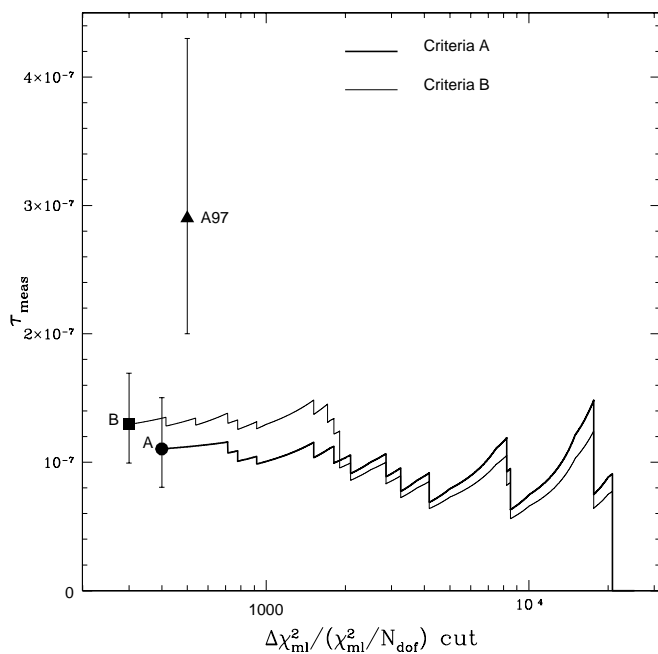
FIG. 11.—Measured microlensing optical depth, plotted as a function of the $\Delta\chi^2/(\chi^2_{ml}/N_{dof})$ cut for selection criteria set A (*thick line*) and set B (*thin line*). Our selected cuts for criteria sets A and B are marked with large filled circles with 1 σ error bars. The optical depth reported in A97 is also shown. See the electronic edition of the Journal for a color version of this figure.

first 2.1 yr of the data set. Events 1, 5, 7, and 9 are all of high quality. Only event 14, 21, and 23 in the following 3.6 yr stand out as having comparable quality. This " qualitative " feel for the events is backed up by the fact that in the first 2.1 yr, 6–7 events were observed, a rate of 2.9–3.3 events yr^{-1}, while for the last 3.6 yr only 7–10 events were observed, a rate of 1.9–2.8 events yr^{-1}. Since the efficiency has not changed drastically over this interval, we conclude that while the exposure increased by a factor of 3.4, the number of events did not. That is, we got " lucky " during the 2.1 yr of A97 and detected more microlensing than average. This possibility was reflected in the large Poisson errors quoted in A97.

Another reason the optical depth reported in A97 is large compared to this work is related to the splitting of the top six fields for analysis, described in § 2. These six fields represented $\sim 27\%$ of our exposure in object-years. Because they were split into two sets of light curves of approximately 1 yr duration, the efficiency was lowered for durations $\gtrsim 100$ days. At least four of the events in the 8 event sample of A97 (events 5, 6, 7, 9) contributed somewhat more to the optical depth than they would have if the top six fields had not been split for analysis. This in itself was not in error, for one would have expected that one or two events would have been missed because of the splitting of the top six fields, and these " missed " events would have counterbalanced the decreased efficiency. By chance, no such events were missed, as is evident in the current analysis, in which the top six fields have been merged and analyzed as full light curves. We estimate that this " small numbers " (Poisson) effect increased the optical depth reported in A97 by $\sim 25\%$.

For reasons discussed in more detail in § 4 (and in Alcock et al. 2000b), our detection efficiency is somewhat higher than in A97. Briefly, we previously neglected a contribution from faint stars with $V > 21.5$, and thus our efficiency in A97 had not yet converged for durations $\gtrsim 100$ days. In

addition, our new normalization, which has been more carefully determined using *HST* data and has more realistically estimated errors, leads to a somewhat increased sensitivity. Together, these effects spuriously increased the optical depth in A97 by $\sim 10\%$ with respect to the current results. This is within our estimated uncertainty.

As mentioned in § 3.3.2, one of the events used in A97 (event 10) is most likely a SN interloper. This interpretation is supported by the presence of an obvious spiral galaxy in our *HST* frames of this event and the fact that it is quite reasonably fitted by a SN Ia light curve. The effect of this interloper spuriously increased the optical depth by $\sim 7\%$ in the 8 event sample, and had no effect on the 6 event sample (which rejected it).

6.1.3. *Errors in Present Analysis*

While the current analysis is the most careful yet performed and a substantial improvement over earlier efforts, there are still a number of errors or potential errors that exist in our results. The errors due to small number statistics are included in the error bars we report (about 30% uncertainty). The errors due to model dependency are explored by considering a range of models. We believe that these are the largest errors in our results. In this short section and in Table 11 we list some other sources of error that might be worth considering in more detail in the future.

Normalization of star-to-object ratio.—The ratio of actual LMC stars to SoDoPHOT objects varies across our fields, and it is very difficult to accurately estimate. We have *HST* images for three areas, and attempt to tie together MACHO object–based photometry to the *HST* star-based photometry to create a unified luminosity function (LF). We estimate a 20% uncertainty in our final results due to uncertainties in this procedure. Issues include the underlying luminosity function, the magnitude calibration of our objects, blending effects in matching the object LF to the stellar LF, and the unknown effects of crowding, seeing, and sky in the template images, among several others.

Selection Criteria.—Since we do not have a complete understanding of the background, and because we examine our data before deciding on the selection criteria, it is possible that we differentiate background and microlensing in an imperfect and/or biased way. We implemented two independent sets of selection criteria as a test of our sensitivity to this bias. We estimate about a 20% uncertainty due to our selection criteria.

Correction to $\hat{t}$.—Blending causes the durations of events to shift from their naive fit values. We chose to correct for this in a statistical manner, and estimate about a 3% uncertainty in this correction. This is due to several factors, but mainly the uncertainty in the true $\hat{t}$ distribution, which is needed to make the correction.

Binary source stars.—Locally, most stars reside in binary or multiple star systems, and it is expected that this is also true of LMC stars. Our LMC luminosity function does not include a correction for this. This is a complicated correction, which will be uncertain, since the binary fraction for LMC stars is not known. We did not make an estimate of the size of this effect, but will consider it in a later paper.

Exotic microlensing.—We do not explicitly add binary-lens microlensing or other exotic lensing into our artificial light curves. Thus, our efficiencies for these are unknown. We did try to explore two sets of selection criteria, to detect any

TABLE 12

MICROLENSING BY STARS

Population	$\tau \times 10^{-8}$	$\langle \hat{t} \rangle$ (days)	$\langle l \rangle$ (kpc)	$\Gamma \times 10^{-8}$ (yr^{-1})	$N_{\mathrm{exp}}(A)$	$N_{\mathrm{exp}}(B)$
Thin disk	0.36	101	1.3	1.7	0.38	0.49
Big thin disk (F)................	0.59	101	1.3	2.7	0.60	0.79
Thick disk.......................	0.20	104	3.6	0.90	0.20	0.26
Spheroid	0.20	129	8.8	0.90	0.19	0.25
LMC disk (with halo)	1.6	120	50	5.8	1.3	1.7
LMC disk (without halo)......	2.6	120	50	9.8	2.2	2.9

NOTE.—This table shows microlensing quantities for various lens populations, with the density and velocity distributions and PDMF described in the text. Here τ is the optical depth, $\langle l \rangle$ is the mean lens distance, and Γ is the total theoretical microlensing rate, but in all cases excluding bright lenses (see text). The expected number of events, N_{exp}, includes our detection efficiency averaged over the $\hat{t}$ distribution. The LMC values are averaged over the locations of our 30 fields. N_{exp} is the number of expected events using either selection criteria set A (13 events) or criteria set B (17 events). Two models of the LMC are considered, one with a dark halo and one without. Lensing from the LMC stellar disk only is shown in this table; lensing from the dark LMC halo is discussed elsewhere.

gross sensitivity of our results to this effect, but a proper calculation should be done in the future.

Others.—There are several other sources of systematic error that have been considered. For example, in the artificial star Monte Carlo, we assume that all flux added goes to the nearest SoDoPHOT object. Direct tests show that this is not true in about 3% of the cases. The effect of this mis-identification is not known, but could be around 3%. Some other small errors are discussed in Alcock et al. (2000b), and a summary is given in Table 11.

Finally, we note that due to the complex nature of systematic errors, it is not straightforward to combine them with each other or with statistical errors. For example, systematic errors can be strongly asymmetric.

We estimate our total systematic error to be in the range of 20%–30%, although even this range is uncertain.

6.2. *Likelihood Analysis and Dark Matter*

We compare the number of detected events and the distribution of observed timescales, $\hat{t}$, with predictions from models of various lens populations. Microlensing can occur when any compact object travels in front of a monitored star, so we expect microlensing events from any population of stars, remnants, or dark compact objects that lie between us and the LMC. Luckily, much is known about the density and velocity distribution of stars and remnants in the Milky Way and LMC. Less is known about the dark halo of the Milky Way (and even less about the dark halo of the LMC), but we can leave the fraction, f, of dark objects that can lens, as well as the masses, m, of these objects, as free parameters, which we determine using a maximum-likelihood analysis. This analysis was done in A97, with six or eight observed microlensing events. We found values of f between 0.15 and 1.0 at the 90% confidence level, and MACHO masses m between 0.1 and 1.0 $M_\odot$. The large uncertainty in these results came mainly from small number statistics, but also from uncertainty in the models. In the current analysis, we have a larger number of events and an improved efficiency determination, so we can reduce the Poisson and some systematic errors. Here we also make improvements to our likelihood analysis, most notably the inclusion of realistic estimates of the stellar lensing background within the likelihood function. We note that the results of this section still depend heavily on the models of the Milky Way and LMC. We will come back to this point in § 7.

6.2.1. *Microlensing Rate*

The microlensing event rate, Γ, is more model dependent than the optical depth, τ. The rate Γ depends on the event timescales via the mass function of MACHOs and their velocity distribution, but the uncertainties in Γ are given purely by Poisson statistics. Thus, Γ is useful in quantifying the errors on any measurement, once a halo model is specified.

The number of observed events is given by a Poisson distribution with a mean of

$$N_{\mathrm{exp}} = E \int_0^\infty \frac{d\Gamma}{d\hat{t}} \, \mathscr{E}(\hat{t}) \, d\hat{t} \,, \qquad (3)$$

where $E = 6.12 \times 10^7$ object-years is our total "exposure," and $d\Gamma/d\hat{t}$ is the total differential microlensing rate,

$$\frac{d\Gamma}{d\hat{t}} = f \frac{d\Gamma}{d\hat{t}} \, (\mathrm{MW\ halo}) + \frac{d\Gamma}{d\hat{t}} \, (\mathrm{thin\ disk})$$

$$+ \frac{d\Gamma}{d\hat{t}} \, (\mathrm{LMC}) + \cdots \,.$$

For a typical dark matter halo (eq. [4], below) consisting of 100% MACHOs, the total rate of microlensing events with $A_{\max} > 1.34$ is given by equation (A2) of A96: $\Gamma \approx 1.6 \times 10^{-6}(m/M_\odot)^{-0.5}$ events star^{-1} yr^{-1}. Thus, if all MACHOs had the same mass and our efficiency were 100%, we would expect about $100(m/M_\odot)^{-0.5}$ events in the present data set. The average timescale of an event scales oppositely, $\langle \hat{t} \rangle \approx 140(m/M_\odot)^{1/2}$ days, since the product of the two gives the optical depth, which is independent of the MACHO masses, $\tau = (\pi/4)\Gamma\langle \hat{t} \rangle$. Thus, although the optical depth is independent of MACHO mass, in a real microlensing experiment, statements about the MACHO content of the halo will depend on the MACHO mass. However, the masses of the lenses are constrained, since we measure the distribution of event timescales.

6.2.2. *Milky Way and LMC Models*

We consider four stellar components and a dark component of the Milky Way, and a stellar and dark component of the LMC. Given our exposure and efficiency, and a model of the density, velocity distribution, and mass function of a lens population, we can calculate the expected microlensing optical depth, microlensing rate, distribution of event durations, and the number of expected events

detected in our experiment. A summary of the results is given in Tables 12 and 13. For the LMC self-lensing model, we note that the rate depends strongly on the position on the sky, so that the values we report depend on the 30 specific fields we monitor.

We model the density of the Milky Way and LMC thin and thick disks as double exponentials,

$$\rho_d = \frac{M_{\rm disk}}{4\pi z_d R_d^2} \exp\left(-\left|\frac{R}{R_d}\right| - \left|\frac{z}{z_d}\right|\right),$$

where z and R are cylindrical coordinates, $M_{\rm disk}$ is the total mass of the disk, z_d is the scale height, and R_d is the scale length. Instead of specifying the total mass, Milky Way disks are often specified by the column density, Σ_0, at the solar circle, $R = R_0 \sim 8.5$ kpc, and the relation is

$$\Sigma_0 = \frac{M_{\rm disk}}{2\pi R_d^2} e^{-R_0/R_d}.$$

For simplicity, we characterize the velocity distribution of a disk as a constant rotation velocity, v_c, with some isotropic dispersion, σ_v, in addition.

For the normal Milky Way thin disk we use the parameters $R_d = 4$ kpc, $z_d = 0.3$ kpc, $\Sigma_0 = 50\ M_\odot$ pc^{-3}, $R_0 = 8.5$ kpc, $v_c = 220$ km s^{-1}, and $\sigma_v = 31$ km s^{-1}. This gives a total thin-disk mass of $M_{\rm disk} = 4.2 \times 10^{10}\ M_\odot$. Later, we will discuss models (e.g., model F) with a maximal thin disk and a smaller dark halo. In that case, we use the above parameters except with $\Sigma_0 = 80\ M_\odot$ pc^{-3}, which gives $M_{\rm disk} = 6.7 \times 10^{10}\ M_\odot$.

For the Milky Way thick disk, we use the parameters $R_d = 4$ kpc, $z_d = 1.0$ kpc, $\Sigma_0 = 4\ M_\odot$ pc^{-3}, $R_0 = 8.5$ kpc, $v_c = 220$ km s^{-1}, and $\sigma_v = 49$ km s^{-1}, for a total mass of $M_{\rm disk} = 3.4 \times 10^9\ M_\odot$.

For the LMC disk, we use the preferred parameters from Gyuk et al. (2000): $R_d = 1.57$ kpc, $z_d = 0.3$ kpc, $v_c = 70$ km s^{-1}, $\sigma_v = 25$ km s^{-1}, and $M_{\rm disk} = 3.0 \times 10^9\ M_\odot$. The LMC disk self-lensing also depends on its distance, $L = 50$ kpc,

inclination, $i = 30°$, and position angle, $\phi = 170°$. These are the parameters we use when considering the LMC disk plus LMC dark halo model. For the pure disk (no LMC halo) case, we conservatively increase $M_{\rm disk}$ to $5 \times 10^9\ M_\odot$, in good agreement with a recent analysis of the LMC rotation curve ($M_{\rm disk} = 5.3 \pm 1.0\ M_\odot$; Alves et al. 1999), corresponding to central surface densities of 190 and 320 $M_\odot$ pc^{-2}, respectively. We do not consider a separate bar component, since the bar mass is strongly limited by the H I kinematics (Kim et al. 1998; Gyuk et al. 2000).

The Milky Way spheroid density is modeled as (Guidice, Mollerach, & Roulet 1994; A96)

$$\rho_{\rm spher} = 1.18 \times 10^{-4}(r/R_0)^{-3.5}\ M_\odot\ \ {\rm pc}^{-3},$$

with no rotation, and an isotropic velocity dispersion of $\sigma_v = 120$ km s^{-1}.

For the LMC, we consider two main cases: (1) pure disk/disk self-lensing, and (2) disk/disk self-lensing plus a LMC dark halo consisting of fraction f of MACHOs, where f is the same fraction used for the Milky Way dark halo. Later, we also consider the possibility of an all-stellar LMC halo.

For the Milky Way dark halo, we consider three models: S, B, and F, which were used in A96 and A97. The density of model S is given by

$$\rho_H(r) = \rho_0 \frac{R_0^2 + a^2}{r^2 + a^2}, \qquad (4)$$

where ρ_H is the halo density, $\rho_0 = 0.0079\ M_\odot$ pc^{-3} is the local dark matter density, r is Galactocentric radius, $R_0 = 8.5$ kpc is the Galactocentric radius of the Sun, and $a = 5$ kpc is the halo core radius.[20] With the standard thin disk, this model has a total rotation speed at 50 kpc of 200 km s^{-1}, with 190 km s^{-1} coming from the halo. We assume an

---

[20] Analysis of carbon star kinematics on the periphery of the LMC disk support a pseudoisothermal density profile for the Galactic dark halo (Alves et al. 1999).

TABLE 13
MAXIMUM-LIKELIHOOD FITS

MODEL/EVENTS (1)	COMMENT (2)	$m_{\rm ML}$ $(M_\odot)$ (3)	$f_{\rm ML}$ (4)	$f_{\rm ML} M_H$ $(10^{10}\ M_\odot)$ (5)	$\tau_{\rm ML}$ (10^{-8}) (6)	$N_{\rm exp}$ MW (7)	$N_{\rm exp}$ LMC Halo (8)	$N_{\rm exp}$ Stars (9)
S/13	standard	$0.60^{+0.28}_{-0.20}$	$0.21^{+0.10}_{-0.07}$	8.5^{+4}_{-3}	10^{+5}_{-3}	9.6	0	3.0
S/13	standard	$0.54^{+0.26}_{-0.18}$	$0.20^{+0.08}_{-0.06}$	$7.9^{+3.4}_{-2.6}$	11^{+5}_{-4}	9.4	1.1	2.1
S/17	standard	$0.79^{+0.32}_{-0.24}$	$0.24^{+0.09}_{-0.08}$	10^{+4}_{-3}	11^{+4}_{-4}	12.7	0	3.9
S/17	standard	$0.72^{+0.30}_{-0.20}$	$0.22^{+0.08}_{-0.07}$	9.1^{+3}_{-3}	12^{+5}_{-4}	12.4	1.4	2.7
B/13	big halo	$0.68^{+0.35}_{-0.22}$	$0.12^{+0.06}_{-0.04}$	8.8^{+4}_{-3}	10^{+5}_{-4}	9.7	0	3.0
B/13	big halo	$0.66^{+0.30}_{-0.22}$	$0.12^{+0.05}_{-0.04}$	8.8^{+4}_{-3}	11^{+5}_{-4}	9.8	0.62	2.1
B/17	big halo	$0.92^{+0.40}_{-0.28}$	$0.14^{+0.06}_{-0.04}$	10^{+4}_{-3}	11^{+5}_{-4}	12.5	0	3.9
B/17	big halo	$0.87^{+0.35}_{-0.26}$	$0.14^{+0.05}_{-0.04}$	10^{+4}_{-3}	12^{+5}_{-4}	12.9	0.78	2.7
F/13	small halo	$0.16^{+0.08}_{-0.05}$	$0.50^{+0.22}_{-0.18}$	10^{+4}_{-4}	10^{+4}_{-3}	9.5	0	3.2
F/13	small halo	$0.19^{+0.09}_{-0.06}$	$0.39^{+0.17}_{-0.13}$	8.0^{+3}_{-3}	11^{+4}_{-3}	7.0	3.3	2.3
F/17	small halo	$0.22^{+0.09}_{-0.06}$	$0.57^{+0.21}_{-0.17}$	11^{+4}_{-4}	11^{+4}_{-3}	12.5	0	4.2
F/17	small halo	$0.25^{+0.10}_{-0.07}$	$0.44^{+0.16}_{-0.13}$	9.0^{+3}_{-3}	11^{+4}_{-4}	9.2	4.3	3.0

NOTE.—Col. (1): Model as defined in A96 and A97 and the number of microlensing candidates used; either 13 from selection criteria set A, or 17 from criteria set B. Model S is given by eq. (4) and has a typical size halo; model B has a halo as large as possible, and model F has a halo as small as possible with a large thin disk. Cols. (3) and (4): Maximum-likelihood MACHO mass and halo fraction from § 6.2.3. Cols. (5) and (6): Implied total mass of MACHOs within 50 kpc of the Galactic center and the resulting halo optical depth. For models with dark LMC halos, the sum of the LMC and Milky Way MACHO optical depth is shown. Col. (7): Number of expected events from the Milky Way halo; col. (8): number of expected events from the LMC halo; col. (9): expected number of events from stars (from Table 12). Every Milky Way model is shown twice, once with a dark LMC halo, and once with the dark LMC halo set to zero. See the text for more explanation.

isotropic Maxwellian distribution of velocities with a one-dimensional rms velocity of 155 km s^{-1}, and assume a δ-function MACHO mass function of arbitrary mass m.[21] Note that we always multiply the above density by the MACHO halo fraction f, implicitly assuming that the remaining fraction $1 - f$ of the halo is filled with some exotic-particle dark matter or other nonlensing matter. Dark halo models B and F are power-law models (Evans 1993; Alcock et al. 1995b), and are discussed in detail in A96 and A97. Model B has a very large dark halo and a standard thin disk, giving a rising rotation curve that reaches 258 km s^{-1} at 50 kpc. Model F has an extremely low mass halo, somewhat inconsistent with the known Galactic rotation curve, and a very massive disk. At 50 kpc, the model F halo contributes 134 km s^{-1} toward a total 160 km s^{-1} rotation speed.

Finally, for the LMC halo we follow Gyuk et al. (2000) and use the same density distribution as model S above, but with a central density of 0.0223 $M_\odot$ pc^{-3}, $a = 2$ kpc, $v_c = 70$ km s^{-1}, and a tidal truncation radius at 11 kpc. In this model, the mass of the LMC halo in the inner 8 kpc is 6×10^9 $M_\odot$, and the total mass of the halo is 9.2×10^9 $M_\odot$. This is a somewhat extreme model, probably larger than allowed by the LMC rotation curve. Like the Milky Way halo, the LMC halo is assumed to consist of a fraction f of MACHOs, all of mass m. It is conceivable that the LMC MACHO halo fraction and makeup differs from the MACHO fraction in the Milky Way halo, and we consider this possibility in the next section. We note that no substantial stellar component of a LMC halo has yet been observed.

For the stellar lensing populations, we integrate the microlensing rate over a mass function. There have been several recent determinations of the present-day mass function (PDMF), but it is not clear that the mass function determined locally is valid for all the stellar populations we model. However, for simplicity we use the PDMF of Gould, Bahcall, & Flynn (1997, without their "binary correction") for all the stellar populations. We did try using this PDMF both with and without their binary correction, and we also tried other PDMFs, but found little difference for the MACHO halo fraction. The choice of PDMF does influence the number of events from disk stars, and to a lesser extent events from spheroid and LMC stars, but these are a relatively small background in the current models. Table 12 shows some properties of the stellar population calculated from the models above. It also shows the expected number of microlensing events from each population found by the likelihood method, and thus including the effect of our efficiency calculation and selection criteria. These results differ to some degree from those presented in A97, for several reasons. First, the models we use are different in some cases, and we are using a different PDMF. Second, and most importantly, we explicitly do not count lenses that are too bright to be detected as microlensing in our experiment. We have an explicit cut at around $V = 17.5$ mag, and so stars brighter than this cannot be found as lenses. Our Monte Carlo shows that this reduces the expected number of thin-disk stellar lensing events by more than half, with smaller

effects for thick-disk, spheroid, etc., and almost no effect for LMC disk lensing. The results displayed in Table 12 use the full Monte Carlo for all stellar distributions.

6.2.3. MACHO Halo Fraction and Mass

We find the most likely values of the halo fraction f and unique MACHO mass m using our set A (13 events) and set B (17 events) and their corresponding efficiencies. The likelihood function is

$$L(m, f) = \exp\left(-N_{\exp}\right) \prod_{i=1}^{N_{\mathrm{obs}}} \left[E\mathscr{E}(\hat{t}_i) \frac{d\Gamma}{d\hat{t}}(\hat{t}_i; m) \right], \quad (5)$$

where

$$\frac{d\Gamma}{d\hat{t}}(\ldots) = f\frac{d\Gamma}{d\hat{t}}(\mathrm{MW\ halo}) + \frac{d\Gamma}{d\hat{t}}(\mathrm{thin\ disk})$$

$$+ \frac{d\Gamma}{d\hat{t}}(\mathrm{thick\ disk}) + \frac{d\Gamma}{d\hat{t}}(\mathrm{spheroid})$$

$$+ \frac{d\Gamma}{d\hat{t}}(\mathrm{bulge}) + \frac{d\Gamma}{d\hat{t}}(\mathrm{LMC\ disk})$$

$$+ f\frac{d\Gamma}{d\hat{t}}(\mathrm{LMC\ halo}) ,$$

and each $(d\Gamma/d\hat{t})(j)$ is the theoretical rate of microlensing derived from model j. The distributions $(d\Gamma/d\hat{t})(i)$ for stellar populations are integrated over a mass function (Gould et al. 1997) as described above, and are calculated using code described in Gyuk et al. (2000).

The results are dependent on the model, so we explore a range of possible halos, including a standard halo (model S from A96 and A97). We also use two other dark halo models. We choose model B from A96 and A97, because it is about as large a halo as the data will allow. We also select model F from A96 and A97, because it has a nearly maximal disk and a very low mass halo, and therefore is as small a halo as the data allow. These models are described in detail in A96. We do not show models A, C, D, or G from A96 and A97, or other possible halo models, since they are in general intermediate between the extremes of models B and F. Model S is a common pseudoisothermal sphere (Griest 1991) with an asymptotic rotation velocity of 220 km s^{-1}, while models B and F are power-law Evans (1993, 1994) models. Table 13 shows the results for all the models, and Figures 12, 13, and 14 show the corresponding likelihood contours.

For model S, the resulting likelihood contours, assuming a δ-function halo mass function, are shown in Figure 12. The probabilities are computed using a Bayesian method with a prior uniform in f and log m. We show likelihood contours for both our 13 event sample and our 17 event sample, and with and without the LMC halo. The best-fit values and errors are given in Table 13. The errors shown in the table are 1 σ errors. The peak of the likelihood contours gives the most probable mass and halo fraction for a given model, and for set A with a LMC halo we find $m_{\mathrm{2D}} = 0.48$ $M_\odot$ and $f_{\mathrm{2D}} = 0.20$. For the corresponding set B, $m_{\mathrm{2D}} = 0.67$ $M_\odot$ and $f_{\mathrm{2D}} = 0.23$.

We calculate the one-dimensional likelihood function by integrating over the other parameter and find (for set A without a LMC dark halo) a most likely MACHO mass of

---

[21] As discussed in A97, a δ-function mass distribution is a reasonable fit to the observed distribution, and more complicated forms are difficult to distinguish with such a small number of events.
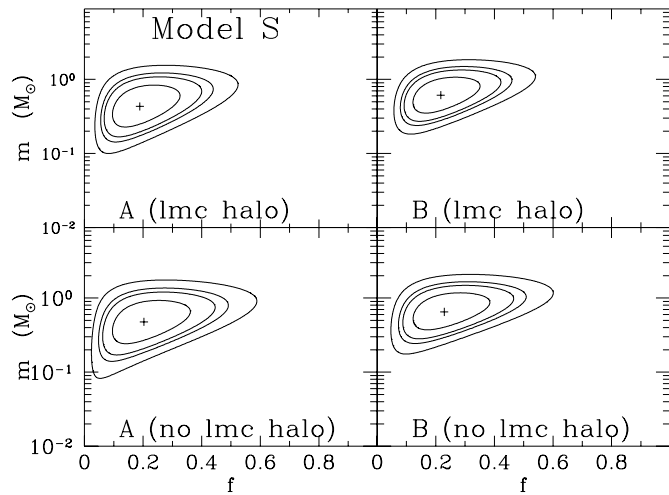
FIG. 12.—Likelihood contours for MACHO mass m and halo fraction f for model S, which has a typical size halo. See A96 for details of the model. The plus sign shows the maximum-likelihood estimate, and the contours enclose regions of 68%, 90%, 95%, and 99% probability. The panels are labeled according to which set of selection criteria (A or B) is used, and whether or not a LMC halo with MACHO fraction f is included.
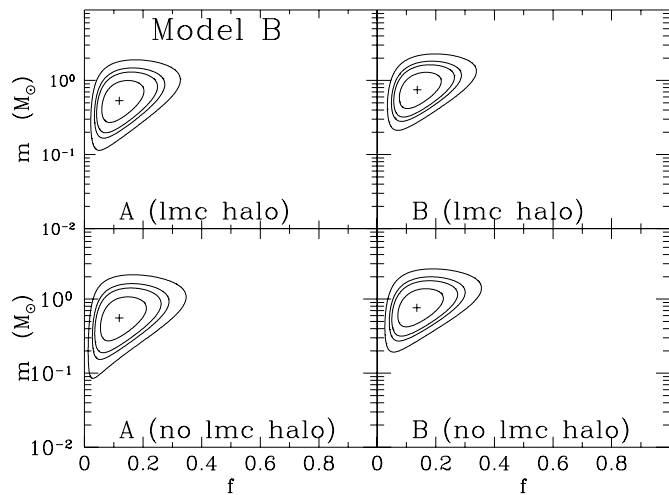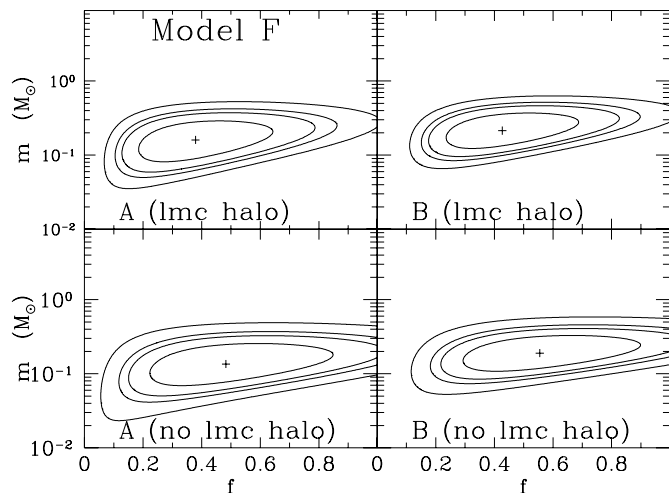

FIG. 13.—Same as Fig. 12, but for model B

FIG. 14.—Same as Fig. 12, but for model F

$m_{\rm ML} = 0.60^{+0.28}_{-0.20}\ M_\odot$, and a most likely halo fraction $f_{\rm ML} = 0.21^{+0.10}_{-0.07}$, where subscript "ML" here indicates maximum likelihood. The errors given are at the 68% confidence level. The values for set B are $m_{\rm ML} = 0.79^{+0.32}_{-0.24}\ M_\odot$ and $f_{\rm ML} = 0.24^{+0.09}_{-0.08}$. For model S, the 95% confidence level contour includes halo fractions from about 8% to about 50%, and MACHOs masses from about 0.12 to 1.1 $M_\odot$, depending on the selection criteria and LMC model used. The likelihood method gives an optical depth for the halo population of $1.1^{+0.5}_{-0.4} \times 10^{-7}$ almost independent of the selection criteria, the LMC model, and the Galactic model.

There are several important comments to be made. First, sets A and B give results that are remarkably similar, implying that the systematic error introduced by our selection criteria methodology is small. The important parameters of estimated MACHO halo fraction are nearly identical using the two different sets of events and efficiency determinations. The estimated typical MACHO mass does vary between the two sets of events, but the values lie within 1 σ of each other. This difference in lens mass comes partially from the rejection of event 22 from set A.

Second, consistent with our optical depth estimates, the values of the halo fraction are approximately a factor of 2 lower than we found in A97. As discussed in § 6.1.2, this is mainly a result of finding more events per unit exposure during the first 2 yr, but it is also due to changes in efficiency, etc. We note that the optical depths reported in Table 13 are the estimated MACHO contribution, and do not include the background of stellar microlensing. The contributions from stellar background are shown in Table 12. The values found here are quite similar to those found directly in § 6.1.

Third, our new confidence intervals are substantially smaller than those of A97 due to the larger number of events. Even though the central values have changed, our new most likely values lie within the A97 90% confidence region. The shift in central values is somewhat larger than one might have naively expected, and while the shift could be statistical, the more likely reason is a previous underestimation of systematic errors.

Next, for model S with a large LMC disk but no LMC dark halo, and set A, we expect a total of 3.0 events from stellar background sources, with the majority coming from LMC self-lensing. For the same model and set B, the number of expected background events is 3.9. In both cases, the predicted number of background events is substantially below the number of detected events. Thus, if these models are correct, the microlensing events are very unlikely to come from the known stellar populations.

For the case of a LMC halo plus LMC disk, LMC disk self-lensing must be smaller, since part of the LMC rotation curve is supported by the halo. In this case, some of the lensing can come from the dark halo. This changes the predictions of MACHO halo fraction, since the LMC halo contributes very little to the total mass of the Milky Way, but relatively more to the microlensing. As shown in Table 13, for model S we find 1.1 events from the LMC halo, and 2.1 background events using set A. For set B we find 1.4 LMC halo events, with 2.7 background stellar events. Again, the expected number of background events is significantly smaller than the number of observed events. When a LMC dark halo is included, the events from the LMC halo count toward dark matter that is not uniformly spread across the sky. The predicted values change from $f = 0.21$ to

0.20 and from $m = 0.60$ to 0.54 $M_\odot$ for set A, and from $f = 0.24$ to 0.22 and from $m = 0.79$ to 0.72 $M_\odot$ for set B. The change in MACHO fraction is small, because our LMC halo has an optical depth of 0.79×10^{-7}, substantially smaller than the 4.7×10^{-7} contributed by model S, and the LMC disk contributes more background when no halo is present. The most likely total mass in MACHOs in the Milky Way dark halo (within 50 kpc) shows an expected drop of about 10% (from 8.5×10^{10} to 7.9×10^{10} $M_\odot$) when a LMC dark halo is included. As we discuss below, with model F, which has a very small Milky Way halo, the change in f and the change in total MACHO mass is much more substantial.

Finally, we note that with a typical halo model such as S, the likelihood contours in all cases rule out a 100% MACHO halo at high significance. This was not true in A97, and is a major result of this work. Strong limits on a MACHO dark matter halo have been given previously for low-mass lenses by the EROS and MACHO collaborations (Aubourg et al. 1995; Alcock et al. 1996b, 1998), and for the solar mass range by the EROS collaboration (Ansari et al. 1997; Afonso et al. 1999; Lasserre et al. 1999). We note that our sensitivity to events longer than a thousand days is small, so we cannot rule out dark matter objects with masses of tens of solar masses.

6.3. Interpretation

Several interesting features can be seen in Table 13 and Figures 12, 13, and 14.

Examination of the likelihood contours shows that with our new data set, the uncertain nature of the Milky Way halo dominates over Poisson error and the systematic error caused by our selection process. For each model, the most likely values and confidence limits are nearly the same, while there are significant differences between models. This is an improvement over A96 and A97, where small number statistics dominated the errors. The values found are typically within 1.5 σ of those reported in A97, but a factor of 2 smaller for the reasons given above.

As noted in A96 and A97, the most likely halo fraction, f, depends strongly on the halo model, with massive halos such as model B giving a small MACHO fraction ($f \sim 13\%$), medium halos such as model S giving medium values ($f \sim 22\%$), and very low mass halos such as model F giving large fractions ($f \sim 40\%$–60%). However, there are some model-independent conclusions that can be drawn. The total predicted mass in MACHOs within 50 kpc (Table 13, col. [5]) is about 9×10^{10} $M_\odot$ for all models. This is again a factor of 2 smaller than reported in A97, for the same reasons. However, for very small halos, such as model F, the total MACHO mass is somewhat dependent on the model of the LMC halo. With no dark LMC halo, masses up to 10×10^{10} $M_\odot$ are found, while with a large dark LMC halo, the prediction drops to 8×10^{10} $M_\odot$. This is because this MW halo has an optical depth of only 1.9×10^{-7}, compared to 0.79×10^{-7} for our LMC halo. Thus, with the large MACHO fraction caused by the very small MW halo, the LMC halo can contribute substantially to microlensing without contributing much to the mass within 50 kpc. Note, however, that when one sums the *total* MACHO contribution to microlensing optical depth (MW halo + LMC halo), the result is $\tau_{ML} = 1.1 \pm 0.4 \times 10^{-7}$, almost completely independent of the MW and LMC halo models. This is shown in column (6) of Table 13. These values and their confidence intervals are simple to interpret statistically, since each model provides a distribution of event durations. Thus, the subtleties discussed in § 6.1 are absent. We note that these values include only the LMC and MW halo contributions, and are close to the values we obtained in our direct estimates of optical depth.

Interestingly, for models S and B, halos consisting of 100% MACHOs are strongly ruled out. Even for the rather extreme model F and no LMC halo, a 100% MACHO halo is ruled out. The only way in which these data are consistent with a 100% MACHO halo is if there is an extremely small MW halo coupled with a very small LMC halo. This is the strongest limit to date on an all-MACHO halo and is a major result of this work. We note that we do not set strong limits on dark matter objects with masses in the tens of solar mass range. However, the 9×10^{10} $M_\odot$ in MACHOs found in this work still represents several times the mass of all known stellar components of the Milky Way. If the bulk of the lenses are located in the halo, then they represent the dominant identified component of our Galaxy, and a major portion of the dark matter.

While τ_{MACHO} and the total mass are fairly model independent, as discussed in A96 and A97, the typical mass of a MACHO, m, is not. Lighter halo models such as F have a smaller implied MACHO mass, $m_{ML} \sim 0.2$ $M_\odot$, while heavier halos such as B have $m_{ML} \sim 0.8$ $M_\odot$, and medium halos such as S give $m_{ML} \sim 0.6$ $M_\odot$. Sets A and B also differ slightly in this parameter. We conclude that our estimate of m is not very robust, but that masses below the brown dwarf limit of 0.08 $M_\odot$ are quite unlikely. Therefore, the nature of the lenses remains unclear.

Finally, using Table 13 and comparing the number of expected events from the MW halo with the number of expected events from known stellar populations, one can ask how strong the case is for any MACHO contribution to the dark matter. For set A, the known stellar background ranges from 2.1 to 3.2 events, depending on the LMC and MW halo model. For set B, the range is 2.7–4.2 stellar events. If our models of the MW thin disk, thick disk, spheroid, and LMC disk are adequate, then it is very unlikely to find 13 (or 17) events when expecting no more than 3.2 (or 4.2) (probability less than 10^{-5} in both cases). We note that the LMC disk we use in the pure-disk model is conservatively large ($M_{disk} = 5 \times 10^9$ $M_\odot$).

The question remains whether a LMC halo could supply the observed microlensing. The halo we use is a good fit to the available data ($M_{halo} = 6 \times 10^9$ $M_\odot$ within 8 kpc), and the rotation curve for this halo plus LMC disk is a good fit to the data (Gyuk et al. 2000). Now, due to the lack of stellar tracers found with the velocity dispersion of ~ 50 km s^{-1} expected for a halo population, we have assumed that this LMC halo is dark. A large dark halo is, of course, typical of dwarf spiral galaxies such as the LMC. Thus, assuming that the halo consists of a fraction f of MACHOs is a reasonable first approximation. Table 13 shows almost no difference in predicted background or other quantities for models S and B having medium to large dark halos; however, for the very small halo model F, nearly half the expected events come from stars or the LMC halo. The likely final halo fraction is still nearly 50%, but with substantially larger error bars. Figure 14 shows, however, that even in this case, a no-MACHO halo is quite unlikely.

Recently, several groups (Aubourg et al. 1999; Weinberg 2000; Kerins & Evans 1999; Gyuk et al. 2000) have con-

sidered lensing by an extended stellar population around the LMC, and have obtained different estimates of the optical depth contribution. Interestingly, Graff et al. (1999) claim tentative ($\sim 2\,\sigma$) detection of a kinematically distinct population. We therefore explore the effect that this would have on our maximum-likelihood analysis by considering the effect of a LMC halo consisting of MACHO fraction f and a Milky Way halo with no MACHO population (thus presumably consisting entirely of exotic elementary particles). The maximum likelihood for such a model gives $f = 1.35^{+0.6}_{-0.4}$ and $m = 0.2^{+0.1}_{-0.08}\ M_\odot$ for set A, and $f = 1.52^{+0.6}_{-0.4}$ and $m = 0.3^{+0.11}_{-0.09}\ M_\odot$ for set B. Thus, a possible non–dark matter explanation for our results is a LMC halo of mass $\sim 9 \times 10^9\ M_\odot$, consisting of stellar-like objects that have not yet been convincingly observed. This value of LMC halo mass is somewhat extreme, although there are published models with masses this high. Clearly, it is important to discover or convincingly rule out the possibility of a large LMC stellar halo.

7. SUMMARY AND DISCUSSION

We have detected between 13 and 17 microlensing events toward the LMC. The implied optical depth, microlensing rate, and MACHO halo fraction are a factor of 2 smaller than found in our previous work, but are consistent with previous results within the errors of small number statistics. The larger number of events allows us to reduce the Poisson error considerably, which along with our improved efficiency analysis and study of sources of systematic error means that the interpretation of the microlensing events is now dominated by uncertainties in the models of the Milky Way and LMC. We find that the number of events is not consistent with known lens sources, and our measured optical depth, $\tau_2^{400} = 1.2^{+0.4}_{-0.3} \times 10^{-7}$, is significantly larger than allowed by known Galactic and LMC stellar populations. The total implied mass in MACHOs within 50 kpc is $\sim 9 \times 10^{10}\ M_\odot$, quite independent of the dark halo model. This is substantially larger than all known stellar components of the Galaxy. However, one of our most important conclusions is that a 100% all-MACHO Milky Way halo is ruled out at the 95% confidence level for a wide range of reasonable models.

One explanation of our results is a Milky Way halo consisting of about 20% MACHOs. Another possibility is an LMC halo that dominates the microlensing, and no MACHOs in the Milky Way halo. The spatial distribution of events makes lensing entirely by a stellar population in the LMC disk or bar less likely, but given the highly uncertain nature of a LMC halo, a previously unknown stellar component or a LMC halo consisting of MACHO dark matter could explain the measured optical depth, the number of observed events, and their spatial distribution on the sky. We note, however, that no known LMC stellar population exhibits kinematics of this nature. It would help

to constrain the kinematics of old populations in the LMC and to look for new populations that could represent the lenses. A direct measurement of the distance to some LMC lenses would be especially useful in distinguishing the two possibilities above.

There is intriguing evidence for a population of white dwarfs (Ibata et al. 2000, 1999; Hodgkin et al. 2000; Méndez & Minniti 2000) in the Hubble Deep Fields (North and South), and in proper motion surveys, consistent with the Milky Way halo hypothesis. These results were spawned primarily by the recent work of Hansen (1999) and Saumon & Jacobson (1999) on low-temperature white dwarf cooling curves, which has been confirmed by Hodgkin et al. (2000). Although the identification of these faint blue objects as halo white dwarfs remains controversial (Flynn et al. 1999), and the small sample sizes restrict an accurate estimate, the suggestion that these white dwarfs could contribute 10%–50% of the dark matter in the Milky Way is certainly stimulating in light of the present work. A Galactic halo composed of $\sim 20\%$ by mass of white dwarfs would seem to be a natural explanation for both the microlensing data and this newly observed population, but the formation of such objects and the chemical enrichment they would cause trigger serious concerns (Fields, Freese, & Graff 2000). A third-epoch HDF image to check the proper motion of these objects, along with additional searches and spectra, should help confirm or rule out this hypothesis.

APPENDIX

This Appendix should be read in conjunction with § 3.1, Table 2, which defines the statistics, and Table 3, which lists the cuts. It gives a description of and rationale for some of the new selection criteria used to select microlensing events.

Some of the important statistics used by both criteria sets A and B are the χ^2 of various fits. For example, a powerful S/N statistic is $\Delta\chi^2 \equiv \chi^2_{\rm const} - \chi^2_{\rm ml}$, where $\chi^2_{\rm const}$ and $\chi^2_{\rm ml}$ are the χ^2 values for the constant-flux and microlensing fits, respectively. The quantity $\Delta\chi^2$ is the effective "significance" of the event summed over all data points. The statistic $\chi^2_{\rm peak}$ refers to the χ^2 of

the microlensing fit in the "peak" region where $A_{\rm fit} > 1.1$. A reduced χ^2 of the microlensing fit outside the interval $t_{\rm max} \pm 2\hat{t}$ is also computed, $\chi^2_{\rm ml\text{-}out}/N_{\rm dof}$. Other useful statistics include the average values of crowding for a star, the microlensing fit values, the magnitude and color, the number of $2\,\sigma$ high points in the peak region, the number of points on the rising and falling side of the peak region, and the number of points outside the peak region.

Based on experience gained in A96 and A97, we have developed a number of new statistics. One such statistic is the fraction of points in the peak that lie above the light curve's median, $N_{\rm hi}/N_{\rm pk}$. This new statistic is helpful in removing events with spurious deviant points associated with crowding/seeing induced fluctuations, satellite/asteroid tracks, and other causes. To further help in removing similar spurious events, we also compute the fraction of points in the peak rejected due to bad PSF measurements, "pkpsfrej," and large crowding values, "pkcrdrej."

We have found it beneficial to concentrate on statistics that help in rejecting variable star background. One such statistic is the ratio of power in the two passbands, "bauto/rauto." The quantity "bauto" is the sum of the absolute values of the flux away from the median in the blue bandpass, and likewise for "rauto" for the red bandpass. Our variable star background generally has more power in the red than in the blue, while our Monte Carlo microlensing events tend to have equal power in both passbands, even when heavily blended (that this is the case is not surprising, given the fact that the color difference between any two stars in the LMC is somewhat restricted). A second new statistic on the ratio of powers in each filter, "pfwsr," uses only points measured simultaneously in both filters and is thus normalized differently from bauto/rauto. To further help reject variable stars, we compute a cross-correlation coefficient between the red and blue filters, "rbcrossout," for which we use only data points that are outside the peak of the event, $t_{\rm max} \pm 1.0\hat{t}$. A powerful new statistic for rejecting variable stars is a robust reduced χ^2 fit to a constant flux, $\chi^2_{\rm robust\text{-}out}/N_{\rm dof}$, also computed outside the interval $t_{\rm max} \pm 1.0\hat{t}$.

Another new S/N statistic is "pfrdev," which is a χ^2 from the baseline counting only upward excursions in the filter window and subtracting a penalty per measurement in the bin, so that $2\,\sigma$ points break even. We subtract the largest single date contribution (1 or 2 points) to ensure robustness against single strongly deviant observations. We also compute a similar χ^2 for the second most significant nonoverlapping filter trigger, pfrdev2. The statistic pfrdev is very similar to $\Delta\chi^2/(\chi^2_{\rm ml}/N_{\rm dof})$, and a comparison of the two on both real data and artificial data yields similar results, even though the latter is derived using the microlensing shape. This gives us added confidence that a cut on $\Delta\chi^2/(\chi^2_{\rm ml}/N_{\rm dof})$ is not very shape dependent. We have opted to use $\Delta\chi^2/(\chi^2_{\rm ml}/N_{\rm dof})$ throughout, but make use of the second peak significant pfrdev2 to ensure the uniqueness of the event. This statistic is useful for eliminating variable stars, but must be used with caution to avoid missing exotic lensing events such as binary lenses or sources that could exhibit a second "bump." Similarly, cuts on $\chi^2_{\rm ml\text{-}out}/N_{\rm dof}$ and $\chi^2_{\rm robust\text{-}out}/N_{\rm dof}$ could potentially bias against detecting widely separated binary microlenses. We ran our selection criteria with and without these cuts to ensure that no exotic lensing events were missed. No additional candidates were found.

REFERENCES

Afonso, C., et al. 1999, A&A, 344, L63
———. 2000, ApJ, 532, 340
Albrow, M. D., et al. 1999, ApJ, 512, 672
Alcock, C., et al. 1995a, ApJ, 454, L125
———. 1995b, ApJ, 449, 28
———. 1996a, ApJ, 461, 84 (A96)
———. 1996b, ApJ, 471, 774
———. 1997a, ApJ, 486, 697 (A97)
———. 1997b, ApJ, 491, L11
———. 1998, ApJ, 499, L9
———. 1999a, ApJ, 518, 44
———. 1999b, PASP, 111, 1539
———. 2000a, ApJ, 541, in press (astro-ph/9907369)
———. 2000b, ApJS, submitted
Alves, D. R., & Nelson, C. 1999, ApJ, submitted
Aubourg, E., Palanque-Delabrouille, N., Salati, P., Spiro, M., & Taillet, R. 1999, A&A, 347, 850
Aubourg, E., et al. 1993, Nature, 365, 623
———. 1995, A&A, 301, 1
Cook, K. H., et al. 1995, in ASP Conf. Ser. 83, Astrophysical Applications of Stellar Pulsation, ed. R. S. Stobie & P. A. Whitelock (San Francisco: ASP), 221
Evans, N. W. 1993, MNRAS, 260, 191
———. 1994, MNRAS, 267, 333
Fields, B. D., Freese, K., & Graff, D. S. 2000, ApJ, 534, 265
Flynn, C., Sommer-Larsen, J., Fuchs, B., Graff, D. S., & Salim, S. 1999, preprint (astro-ph/9912264)
Gates, E., Gyuk, G., & Turner, M. 1995, Phys. Rev. Lett., 74, 3724
Gould, A. 1993, ApJ, 404, 451
Gould, A., Bahcall, J., & Flynn, C. 1997, ApJ, 482, 913
Graff, D., Gould, A., Suntzeff, N., Schommer, B., & Hardy, E. 1999, ApJ, submitted (preprint astro-ph/9910360)
Griest, K. 1991, ApJ, 366, 412
Guidice, G. F., Mollerach, S., & Roulet, E. 1994, Phys. Rev. D, 50, 2406
Gyuk, G., Dalal, N., & Griest, K. 2000, ApJ, 535, 90
Han, C., & Gould, A. 1995, ApJ, 449, 521
Hansen, B. M. S. 1999, ApJ, 520, 680

Hart, J., et al. 1996, PASP, 108, 220
Hodgkin, S. T., Oppenheimer, N. C., Hambly, R. F., Jameson, R. F., Smartt, S. J., & Steele, I. A. 2000, Nature, 403, 57
Ibata, R., Irwin, M., Bienayme, O., Scholz, R., & Guibert, J. 2000, ApJ, 532, L41
Ibata, R. A., Richer, H. B., Gilliland, R. L., & Scott, D. 1999, ApJ, 524, L95
Kerins, E. J., & Evans, N. W. 1999, ApJ, 517, 734
Kim, S., Staveley-Smith, L., Dopita, M. A., Freeman, K. C., Sault, R. J., Kesteven, M. J., & McConnell, D. 1998, ApJ, 503, 674
Lasserre, T., et al. 1999, preprint (astro-ph/9909505)
Marshall, S. L., et al. 1994, in IAU Symp. 161, Astronomy from Wide Field Imaging, ed. H. T. MacGillivray, et al. (Dordrecht: Kluwer), 67
Méndez, R. A., & Minniti, D. 2000, ApJ, 529, 911
Paczyński, B. 1986, ApJ, 304, 1
———. 1996, ARA&A, 34, 419
Palanque-Delabrouille, N., et al. 1998, A&A, 332, 1
Phillips, M. M. 1993, ApJ, 413, L105
Refsdal, S. 1964, MNRAS, 128, 295
Renault, C., et al. 1997, A&A, 324, L69
Rhie, S. H., Becker, A. C., Bennett, D. P., Fragile, P. C., Johnson, B. R., King, L. J., Peterson, B. A., & Quinn, J. 1999, ApJ, 522, 1037
Riess, A. G., Press, W. H., & Kirshner, R. P. 1996, ApJ, 473, 88
Roscherr, B., & Schaefer, B. 1999, preprint (astro-ph/9909162)
Roulet, E., & Mollerach, S. 1996, Phys. Rep., 279, 68
Salati, P., Taillet, R., Aubourg, E., Palanque-Delabrouille, N., & Spiro, M. 1999, A&A, 350, L57
Saumon, D., & Jacobson, S. 1999, ApJ, 511, L107
Schlegel, E. M. 1990, MNRAS, 244, 269
Stathakis, R. A., & Sadler, E. M. 1991, MNRAS, 250, 786
Stubbs, C. W., et al. 1993, in Proc SPIE, 1900, 192
Udalski, A., Kubiak, M., & Szymański, M. 1997, Acta Astron., 47, 319
Udalski, A., Kubiak, M., Szymański, M., Pietrzyński, G., Woźniak, P., & Żebruń, K. 1998, Acta Astron., 48, 431
Vandehei, T. 2000, Ph.D. thesis, Univ. California, San Diego
Weinberg, M. 2000, ApJ, 532, 922
Woods, E., & Loeb, A. 1998, ApJ, 508, 760